

PROPERTIES OF THE TRANS-NEPTUNIAN BELT: STATISTICS FROM THE CANADA-FRANCE-HAWAII TELESCOPE SURVEY¹

CHADWICK A. TRUJILLO² AND DAVID C. JEWITT

Institute for Astronomy, 2680 Woodlawn Drive, Honolulu, HI 96822; chad@ifa.hawaii.edu, jewitt@ifa.hawaii.edu

AND

JANE X. LUU

Leiden Observatory, Postbus 9513, NL-2300 RA Leiden, Netherlands; luu@strw.leidenuniv.nl

Received 2000 September 18; accepted 2001 April 2

ABSTRACT

We present the results of a wide-field survey designed to measure the size, inclination, and radial distributions of Kuiper Belt objects (KBOs). The survey found 86 KBOs in 73 deg² observed to limiting red magnitude of 23.7 using the Canada-France-Hawaii Telescope and the 12K × 8K CCD mosaic camera. For the first time, both ecliptic and off-ecliptic fields were examined to more accurately constrain the inclination distribution of the KBOs. The survey data were processed using an automatic moving-object detection algorithm, allowing a careful characterization of the biases involved. In this work, we quantify fundamental parameters of the classical KBOs (CKBOs), the most numerous objects found in our sample, using the new data and a maximum likelihood simulation. Deriving results from our best-fit model, we find that the size distribution follows a differential power law with exponent $q = 4.0^{+0.6}_{-0.5}$ (1 σ , or 68.27% confidence). In addition, the CKBOs inhabit a very thick disk consistent with a Gaussian distribution of inclinations with a half-width of $i_{1/2} = 20^{+6}_{-4}$ deg (1 σ). We estimate that there are $N_{\text{CKBO}}(D > 100 \text{ km}) = 3.8^{+2.9}_{-1.5} \times 10^4$ (1 σ) CKBOs larger than 100 km in diameter. We also find compelling evidence for an outer edge to the CKBOs at heliocentric distances $R = 50$ AU.

Key words: Kuiper belt — minor planets, asteroids — solar system: formation

On-line material: machine-readable table

1. INTRODUCTION

The rate of discovery of Kuiper Belt objects (KBOs) has increased dramatically since the first member (1992 QB₁) was found (Jewitt & Luu 1993). As of 2000 December, ~400 KBOs were known. These bodies exist in three dynamical classes (Jewitt, Luu, & Trujillo 1998): (1) the classical KBOs (CKBOs) occupy nearly circular (eccentricities $e < 0.25$) orbits with semimajor axes $41 \text{ AU} \lesssim a \lesssim 46 \text{ AU}$, and they constitute ~70% of the observed population; (2) the resonant KBOs occupy mean motion resonances with Neptune, such as the 3:2 ($a \approx 39.4 \text{ AU}$) and 2:1 ($a \approx 47.8 \text{ AU}$), and comprise ~20% of the known objects; (3) the scattered KBOs represent only ~10% of the known KBOs but possess the most extreme orbits, with median semimajor axis $a \sim 90 \text{ AU}$ and eccentricity $e \sim 0.6$, presumably due to a weak interaction with Neptune (Duncan & Levison 1997; Luu et al. 1997; Trujillo, Jewitt, & Luu 2000). Although these classes are now well established, only rudimentary information has been collected about their populations. One reason is that only a fraction of the known KBOs were discovered in well-parameterized surveys that have been published in the open literature (principally Jewitt & Luu 1993 [one KBO], Jewitt & Luu 1995 [17 KBOs], Irwin, Tremaine, & Żytkow 1995 [two KBOs], Jewitt, Luu, & Chen 1996 [15 KBOs], Gladman et al. 1998 [five KBOs],

Jewitt et al. 1998 [13 KBOs], and Chiang & Brown 1999 [two KBOs]). In this work, we characterize the fundamental parameters of the CKBOs: the size distribution, inclination distribution, and radial distribution using a large sample (86 KBOs) discovered in a well-characterized survey.

The quintessential measurement of the size distribution relies on the cumulative luminosity function (CLF). The CLF describes the number of KBOs per square degree (Σ) near the ecliptic as a function of apparent red magnitude (m_R). It is fitted with the relation $\log \Sigma = \alpha(m_R - m_0)$, where m_0 is the red magnitude at which $\Sigma = 1 \text{ KBO deg}^{-2}$. The slope (α) is related to the size distribution (described below). Although many different works have considered the CLF, two papers are responsible for discovering the majority of KBOs found in published surveys: Jewitt et al. (1996) and Jewitt et al. (1998). The former constrained the CLF over a 1.6 mag range ($23.2 < m_R < 24.8$) with 15 discovered KBOs, while the latter covered a complementary 2.5 mag range ($20.5 < m_R < 23.0$), discovering 13 objects. Jewitt et al. (1998) measured the CLF produced from these two data sets and found $\alpha = 0.58 \pm 0.05$ and $m_0 = 23.27 \pm 0.11$. Gladman et al. (1998) criticized this work on two main counts: (1) they believed that Jewitt et al. (1996) underestimated the number of KBOs, and (2) the fit in the Jewitt et al. (1998) survey used a least-squares approach that assumed Gaussian errors rather than Poisson errors. Gladman et al. found five additional KBOs and reanalyzed the CLF using a Poissonian maximum likelihood method to refit the CLF to (1) the Jewitt et al. (1998) data without the Jewitt et al. (1996) data and (2) a fit to the six different surveys available at the time except for Tombaugh (1961), Kowal (1989), and Jewitt et al. (1996). Both these fits were steeper but formally consistent with the original Jewitt et al. (1998) data at the

¹ Based on observations collected at Canada-France-Hawaii Telescope, which is operated by the National Research Council of Canada, the Centre National de la Recherche Scientifique of France, and the University of Hawaii.

² Current address: Division of Geological and Planetary Sciences, Mail Stop 150-21, California Institute of Technology, Pasadena, CA 91125; chad@gps.caltech.edu.

$\sim 1.5 \sigma$ level: (1) $\alpha = 0.72^{+0.30}_{-0.26}$ and $m_0 = 23.3^{+0.2}_{-0.4}$ and (2) $\alpha = 0.76^{+0.10}_{-0.11}$ and $m_0 = 23.40^{+0.20}_{-0.18}$. Chiang & Brown (1999) found a flatter size distribution of $\alpha = 0.52 \pm 0.05$ and $m_0 = 23.5 \pm 0.06$, much closer to the Jewitt et al. (1998) result. They observed that the steep size distribution reported by Gladman et al. (1998) was an artifact of their selective exclusion of part of the available survey data, not of their use of a different fitting method. The first goal of this work is to measure the CLF and additionally constrain the power-law slope of the size distribution using a single well-characterized survey and a maximum likelihood simulation that allows for the correction of observational biases.

An accurate characterization of the inclination distribution of the KBOs is critical to understanding the dynamical history of the outer solar system since the era of planetesimal formation. We expect that the KBOs formed by accretion in a very thin disk of particles with a small internal velocity dispersion (see, e.g., Kenyon & Luu 1998; Hahn & Malhotra 1999) and a correspondingly small inclination distribution. However, the velocity dispersion indicated by the inclination distribution in the present-day Kuiper Belt is large. Jewitt et al. (1996) measured the *apparent* half-width of the Kuiper Belt inclination distribution to be $\sim 5^\circ$. They noted a strong bias against observing high-inclination objects in ecliptic surveys, and they estimated the true distribution to be much thicker, with an inclination distribution half-width of $\gtrsim 15^\circ$, corresponding to a vertical velocity dispersion of $\sim 1 \text{ km s}^{-1}$. Several conjectures have been advanced to explain the thickness of the Kuiper Belt: Earth-mass planetesimals may have been scattered through the belt in the late stages of the planet formation era, exciting the Kuiper Belt (Morbidelli & Valsecchi 1997; Petit, Morbidelli, & Valsecchi 1999); stellar encounters may have enhanced the velocity dispersion of the distant KBOs (Ida, Larwood, & Burkert 2000); and the velocity dispersion of small bodies tends to grow to roughly equal the escape speed of the bodies contributing the most mass (the large bodies for size distributions with $q < 4$) in the belt (Aarseth, Lin, & Palmer 1993). As there is much speculation about the origin of the large velocity dispersion of the Kuiper Belt, but only one published measurement (Jewitt et al. 1996), the second goal of this work is to accurately quantify the inclination distribution from our large sample of objects.

The radial extent of the classical Kuiper Belt has not been well constrained. None of the CKBOs have been discovered beyond $R \approx 50 \text{ AU}$. This trend was first noted by Dones (1997), who suggested that the 50–75 AU region may be depleted; he found the results of a Monte Carlo simulation of CKBOs drawn from a rather flat differential size distribution (power-law index $q = 3$) to be inconsistent with the observations of the six CKBOs discovered by Jewitt et al. (1996). Jewitt et al. (1998) discovered all of their KBOs at heliocentric distances $R < 46 \text{ AU}$. In the absence of other effects, one should expect to find fewer bodies with $R > 50 \text{ AU}$ than with $R \sim 40 \text{ AU}$, as the former are about a magnitude fainter than the latter. However, through the use of a Monte Carlo model they demonstrated that the bias against objects beyond 50 AU is not strong enough to explain the distribution of discovery distances. They speculated that the lack of bodies discovered beyond 50 AU could be caused by a combination of (1) a decrease in the maximum KBO size (and reduction in the brightest and most detectable objects) beyond 50 AU, or (2) the size distribution might steepen beyond 50 AU, putting more of the mass in the smaller, less

detectable bodies. They also suggested that the lack of $R > 50 \text{ AU}$ objects could be explained by an outer edge to the classical Kuiper Belt at 50 AU.

Two later papers questioned the existence of an edge to the Kuiper Belt near 50 AU. Gladman et al. (1998) suggested that the number of objects expected to be discovered beyond 50 AU is highly dependent on the size distribution because steep size distributions reduce the number of large (bright) bodies relative to small (faint) bodies. Gladman et al. adopted a relatively steep distribution ($q = 4.65$), and found no significant evidence of a truncated belt. Chiang & Brown (1999) found that 8%–13% of the ~ 100 objects known at the time should have been found beyond 50 AU, and suggested that this precludes the presence of a density enhancement beyond 50 AU, but could not definitively rule out a density deficit. Allen, Bernstein, & Malhotra (2001) have also recently reported the detection of an outer edge to the Kuiper Belt as have Trujillo & Brown (2001). The third goal of the present work is to test the distribution of the discovery distances for the presence of an outer edge to the Kuiper Belt.

2. SURVEY DATA

Observations were made at the 3.6 m diameter Canada-France-Hawaii Telescope using the $12,288 \times 8192$, $15 \mu\text{m}$ pixel mosaic CCD (CFHT 12K; Cuillandre et al. 2000). Built at the University of Hawaii (UH), the CFHT 12K comprises 12 edge-abutted, thinned, high quantum efficiency (QE ~ 0.75), 4096×2048 pixel Lincoln Laboratory CCDs. It is currently the largest close-packed CCD camera in the world. When mounted at the CFHT f/4 prime focus, the camera yields a plate scale of $0''.206 \text{ pixel}^{-1}$, corresponding to a 0.330 deg^2 field of view in each 200 Mbyte image. Images were taken through a Mould R filter, with a central wavelength of 6581 \AA and a bandwidth of 1251 \AA . Instrumental parameters of the survey are summarized in Table 1.

Observations were taken within a few days of new Moon under photometric conditions during three periods: 1999 February 10–15, 1999 September 5–8, and 2000 March 31–April 3. Fields were imaged at air masses less than 1.7 and were within 1.5 hr of opposition. We chose to use short 180 s exposures at the CFHT to maximize area coverage

TABLE 1
CFHT SURVEY PARAMETERS

Quantity	CFHT 3.6 m
Focal ratio	f/4
Instrument	CFHT 12K \times 8K mosaic
Plate scale (arcsec pixel $^{-1}$)	0.206
North-south extent (deg)	0.47
East-west extent (deg)	0.70
Field area (deg 2)	0.330
Total area (deg 2)	73
Integration time (s)	180
Readout time (s)	60
m_{R50}^a	23.7
θ^b (arcsec)	0.7–1.1
Filter	R
Quantum efficiency	0.75

^a The red magnitude at which detection efficiency reaches half of the maximum efficiency.

^b The typical full width at half-maximum of stellar sources for the surveys.

and detection statistics. All discovered objects were accessible for recovery at the UH 2.2 m telescope during comparable seeing conditions with exposure times of less than 600 s. Each field was imaged three times (a “field triplet”), with about 1 hr time base between exposures. Fields imaged appear in Figures 1, 2, and 3, and in Table 2. The CFHT observations were taken at three ecliptic latitudes $\beta = 0^\circ$, 10° , and 20° to probe the inclination distribution of the KBOs (see § 4).

Photometric calibrations were obtained from Landolt (1992) standard stars imaged several times on each chip. Three CFHT 12K chips of poor quality were replaced between the 1999 February and 1999 September runs. The positions of four other CFHT 12K chips within the focal-plane array were changed to move the cosmetically superior chips toward the center of the camera. The photometric calibration accounts for these changes, as shown in Table 3,

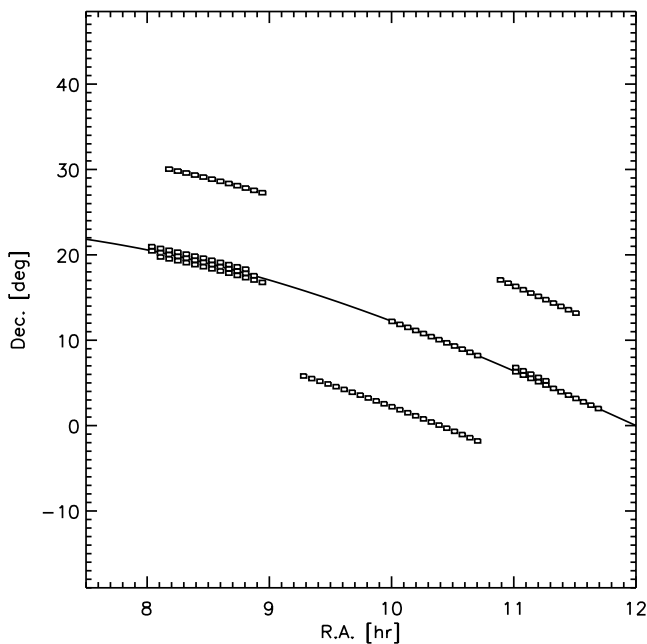


FIG. 1.—Fields imaged in 1999 February. The ecliptic is denoted by a solid line.

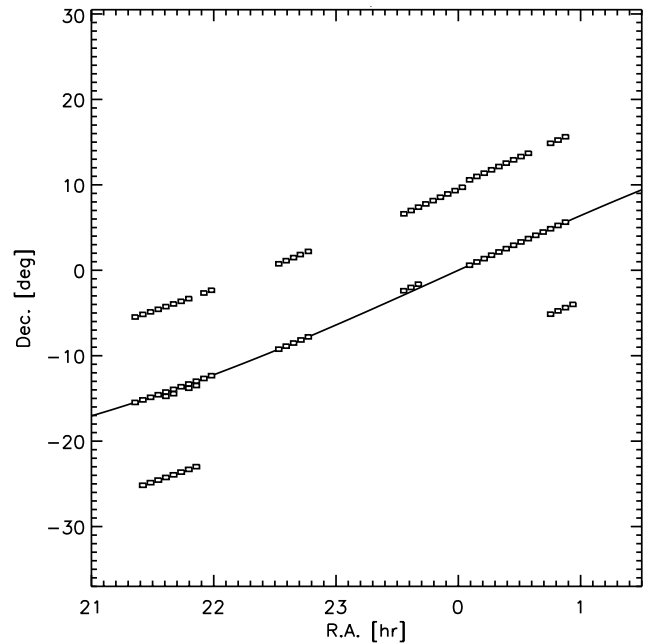


FIG. 2.—Same as Fig. 1, but for 1999 September

containing the measured photometric zero points of the chips. In addition, chip 6 was not used in 1999 February, because of its extremely poor cosmetic quality. The area covered in the fields from 1999 February was corrected for this 8% reduction in field of view. The area imaged in 2000 March included some small field overlap (6%), resulting in a minor correction applied to the reported total area surveyed.

Each of the 12 CCDs in the CFHT 12K functions as an individual detector, with its own characteristic bias level, flat field, gain level, and orientation (at the $\sim 1^\circ$ level). The bias level for each chip was estimated using the row-by-row median of the overscan region. Flat fields were constructed from a combination of (1) the median of normalized bias-subtracted twilight flat fields and (2) a median of bias-subtracted data frames, with a clipping algorithm used to remove excess counts due to bright stars. Fields were analyzed by subtracting the overscan region, dividing by

TABLE 2
CFHT FIELD CENTERS

ID	UT Date	UT Times	β^a	α^b	δ^c	θ^d	Objects	Chip
476758o	1999 Feb 10	1017, 1116, 1223	0.0	11 00 58	06 18 15	g	1999 CY ₁₁₈	03
476759o	1999 Feb 10	1022, 1121, 1228	0.0	11 04 41	05 54 46	g	1999 CZ ₁₁₈	05
476760o	1999 Feb 10	1027, 1127, 1233	0.0	11 08 24	05 31 46	g		
476761o	1999 Feb 10	1032, 1131, 1238	0.0	11 12 06	05 08 30	g	1999 CA ₁₁₉	03
							1999 CW ₁₁₈	04
							1999 CB ₁₁₉	07
476762o	1999 Feb 10	1037, 1136, 1243	0.0	11 15 47	04 45 05	g	1999 CC ₁₁₉	07

NOTE.—Fields imaged with the CFHT 12K Mosaic camera. Fields were imaged in triplets, with UT times given for each image. KBOs found are listed after the field of discovery. If more than one KBO was found in each field, they are listed on successive lines. Table 2 is presented in its entirety in the electronic edition of the *Astronomical Journal*. A portion is shown here for guidance regarding its form and content.

^a J2000 ecliptic latitude, in degrees.

^b J2000 right ascension, in hours, minutes, and seconds.

^c J2000 declination, in degrees, arcminutes, and arcseconds.

^d Seeing category: “g,” “m,” and “p” represent the good (≤ 0.8), medium (> 0.8 and < 1.0), and poor (≥ 1.0) seeing cases, respectively. The efficiency functions for each of these cases are presented in Table 4.

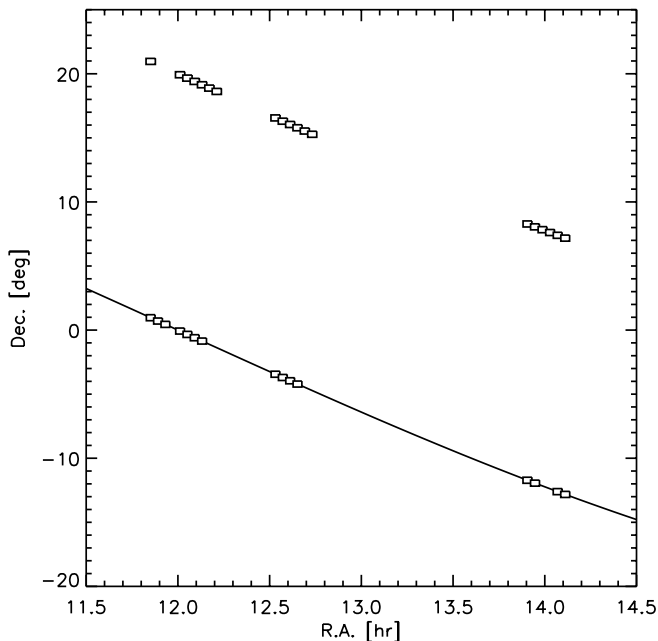


FIG. 3.—Same as Fig. 1, but for 2000 March

the composite flats, and searching for moving objects using our Moving Object Detection Software (MODS; Trujillo & Jewitt 1998). We rejected bad pixels through the use of a bad-pixel mask.

Artificial moving objects were added to the data to quantify the sensitivity of the moving-object detection procedure (Trujillo & Jewitt 1998). The seeing during the survey typically varied from $0''.7$ to $1''.1$ (FWHM). Accordingly, we subdivided and analyzed the data in three groups based on the seeing. Artificial moving objects were added to bias-subtracted twilight sky-flattened images, with profiles matched to the characteristic point-spread function for each image group. These images were then passed through the data analysis pipeline. The detection efficiency was found to be uniform with respect to sky-plane speed in the $1''$ – $10''$ hr^{-1} range. At opposition, the apparent speed in arcseconds per hour, $\dot{\theta}$, of an object is dominated by the parallac-

tic motion of Earth, and it follows

$$\dot{\theta} \approx 148 \left(\frac{1 - R^{-0.5}}{R - 1} \right), \quad (1)$$

where R is heliocentric distance in AU (Luu & Jewitt 1988). From equation (1), our speed-limit criterion for the survey, $1'' \text{ hr}^{-1} < \dot{\theta} < 10'' \text{ hr}^{-1}$, corresponds to opposition heliocentric distances $10 \text{ AU} \lesssim R \lesssim 140 \text{ AU}$, with efficiency variations within this range due only to object brightness and seeing.

The magnitude-dependent efficiency function was fitted by

$$\epsilon = \frac{\epsilon_{\max}}{2} \left[\tanh \left(\frac{m_{R50} - m_R}{\sigma} \right) + 1 \right], \quad (2)$$

where $0 < \epsilon < 1$ is the efficiency with which objects of red magnitude m_R are detected, ϵ_{\max} is the maximum efficiency, m_{R50} is the magnitude at which $\epsilon = \epsilon_{\max}/2$, and σ mag is the characteristic range over which the efficiency drops from ϵ_{\max} to zero. Table 4 shows the efficiency function derived for each seeing category, along with an average of the seeing cases, weighted by sky area imaged, applicable to the entire data set. The efficiency function is known to greater precision than the ~ 0.1 mag uncertainty on our discovery photometry. Changes to the efficiency function of less than 0.1 mag produce no significant variation in our results for the size or inclination distributions.

The MODS software, running on two Sun Ultra 10 computers, was fast enough to efficiently search for the KBOs in near-real time, so that newly detected objects could be quickly discovered and reimaged. We imaged ~ 35 field triplets each night at the CFHT, corresponding to ~ 20 Gbyte of raw data collected per night, plus several more gigabytes for flat fields and standard stars. Eighty-six KBOs were found in the CFHT survey, two of which were serendipitous redetections of known objects. The discovery conditions of the detected objects appear in Table 5. Photometry was performed using a $2''.5$ diameter synthetic aperture for discovery data, resulting in median photometric error of 0.15 mag and a maximum photometric error of 0.3 for the faintest objects. Our results are unaffected by this error; randomly introducing ± 0.15 mag errors in our

TABLE 3
CFHT 12K PHOTOMETRIC CALIBRATION

Chip	$m_0 \pm \sigma$	N	Chip	$m_0 \pm \sigma$	N
1999 February:			1999 September and 2000 March:		
00.....	25.63 ± 0.03	2	00 (04 in 1999 Feb).....	26.08 ± 0.08	6
01.....	25.74 ± 0.08	4	01	25.74 ± 0.08	4
02.....	25.78 ± 0.08	7	02	25.78 ± 0.08	7
03.....	26.07 ± 0.10	8	03 ^a	25.99 ± 0.12	3
04.....	26.08 ± 0.08	6	04 (05 in 1999 Feb).....	26.06 ± 0.09	4
05.....	26.06 ± 0.09	4	05 (11 in 1999 Feb).....	26.13 ± 0.04	2
06.....	Not used		06 ^a	25.56 ± 0.03	5
07.....	25.79 ± 0.04	4	07	25.79 ± 0.04	4
08.....	26.00 ± 0.10	17	08	26.00 ± 0.10	17
09.....	25.98 ± 0.05	6	09	25.98 ± 0.05	6
10.....	26.03 ± 0.01	2	10 ^a	25.49 ± 0.06	2
11.....	26.13 ± 0.04	2	11 (03 in 1999 Feb).....	26.07 ± 0.10	8

NOTE.—Zero points were consistent between observing runs; however, three chips were replaced and several of the remaining chips were shifted in position and renumbered after the 1999 February run.

^a New chip added after 1999 February run.

TABLE 4
CFHT SURVEY EFFICIENCY

Quantity	Good	Medium	Poor	Global
Median PSF FWHM (arcsec).....	0.76	0.90	1.07	0.84
PSF FWHM range (arcsec)	0.56–0.80	0.80–1.00	1.00–1.40	0.56–1.40
e_{\max}	0.83	0.83	0.83	0.83
m_{R50}	24.01	23.64	23.35	23.74
σ	0.29	0.38	0.47	0.48
Fields imaged	95	89	49	233

simulations (described later) and ± 0.3 mag errors in the faintest objects produced no statistically significant change. Trailing loss was insignificant, as the KBOs moved only 0".15 during our integration.

2.1. Recovery Observations and Orbits

Extensive efforts were made to recover all objects using the UH 2.2 m telescope. Attempts were made to recover the objects 1 week after discovery, then 1, 2, and 3 months after discovery. Most of these attempts were successful, as demonstrated by the fact that 79 of the 86 CFHT objects were recovered. The loss of seven objects is the result of unusually poor weather during the 1999 March–May recovery period. Only six of the 79 recovered objects have arc lengths shorter than 30 days as of 2000 December 1.

Orbits derived from the discovery and recovery data appear in Table 6. The listed elements are those computed by B. Marsden of the Minor Planet Center. We also benefited from orbital element calculations by D. Tholen (University of Hawaii). Both sources produced comparable orbital solutions to the astrometric data.

With only first opposition observations, the inclination and heliocentric distance at discovery can be well deter-

mined for nearly all KBOs, as depicted in Figure 4. We find that the semimajor-axis and eccentricity determinations are less reliable but are usually good enough to classify the objects as either classical, resonance, or scattered KBOs, as depicted in Figure 5. We find that six out of 36 (17%) of the objects exhibit orbital changes large enough for their dynamical classification to change from the first opposition to the second opposition. Randomly rejecting 17% of our sample (to simulate misclassification) does not significantly change the results. In addition, rejection of all but the multiopposition objects does not significantly change our results; as expected, the total number of KBOs estimated decreased by a factor of ~ 2 and error bars increased by a factor of $\sim \sqrt{2}$ due to the sample size reduction. The eccentricity and semimajor axes of all objects with $a < 50$ AU (this includes all classical KBOs) appear in Figure 6.

In the next two sections, we use our observations to constrain three fundamental quantities of the classical KBOs: (1) the size distribution index, q , (2) the half-width of the inclination distribution, $i_{1/2}$, and (3) the total number of CKBOs larger than 100 km in diameter, $N_{\text{CKBO}}(D > 100 \text{ km})$. The quantities $i_{1/2}$ and q are uncorrelated, as the

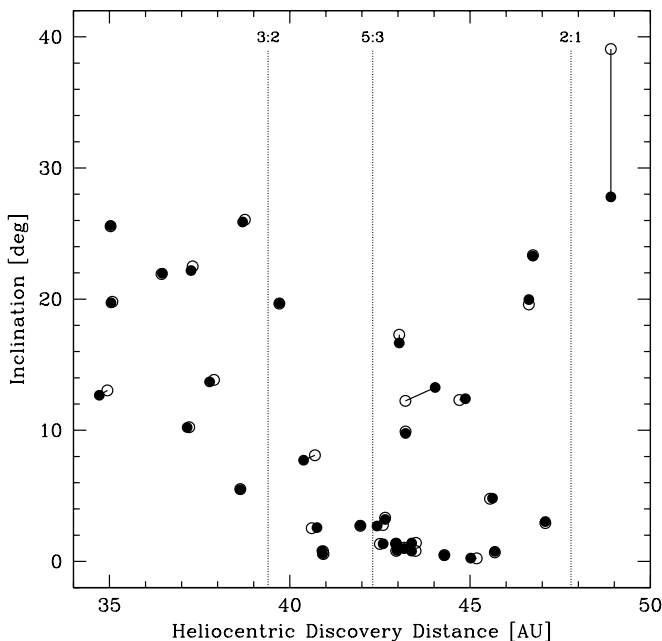


FIG. 4.—Inclination vs. discovery distance of all multiopposition KBOs. The open circles represent quantities determined from < 90 day time base during the first opposition. The connected filled circles represent the orbital solution including second opposition observations. Note that for all objects except one, quantities are well determined during the first opposition.

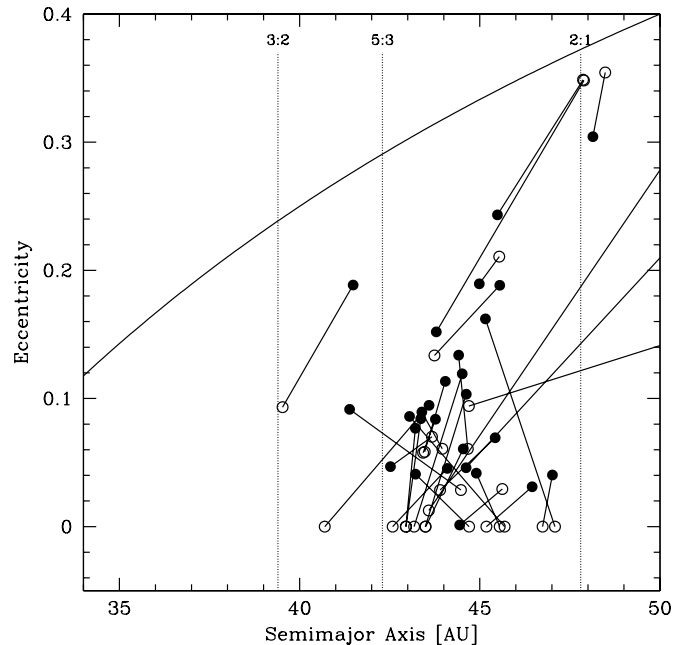


FIG. 5.—Eccentricity vs. semimajor axis of all multiopposition KBOs with $a < 50$ AU. The open circles represent the orbits determined during the first opposition. The connected filled circles show the orbital elements computed including second opposition observations. Two CKBOs were reclassified as scattered KBOs, and one scattered KBO was reclassified as a CKBO. In addition, three resonant KBOs were reclassified as nonresonant objects.

TABLE 5
CFHT DISCOVERY CONDITIONS

ID	β (deg)	Date	R (AU)	Δ (AU)	α' (deg)	$m_R \pm \sigma^a$	$m_R(1, 1, 0)^b$	D^c (km)	MPC Name
C17000.....	+10	1999 Feb 15	41.161	42.085	0.5	21.36 \pm 0.15	5.16	527	1999 CC ₁₅₈
C71710.....	0.0	1999 Feb 10	47.562	48.474	0.4	21.08 \pm 0.17	4.27	797	1999 CD ₁₅₈
C72105.....	0.0	1999 Feb 10	37.694	38.631	0.5	22.80 \pm 0.09	6.99	228	1999 CV ₁₁₈
C72505.....	0.0	1999 Feb 10	46.521	47.477	0.3	23.54 \pm 0.32	6.82	246	1999 CP ₁₅₃
C72600.....	0.0	1999 Feb 10	37.713	38.671	0.4	23.76 \pm 0.14	7.94	146	1999 CK ₁₅₈
C75803.....	0.0	1999 Feb 10	34.141	35.053	0.6	23.61 \pm 0.13	8.22	129	1999 CY ₁₁₈
C75905.....	0.0	1999 Feb 10	45.106	46.010	0.5	24.40 \pm 0.27	7.82	155	1999 CZ ₁₁₈
C76103.....	0.0	1999 Feb 10	44.262	45.153	0.5	24.11 \pm 0.26	7.61	171	1999 CA ₁₁₉
C76104.....	0.0	1999 Feb 10	42.565	43.455	0.6	24.05 \pm 0.21	7.72	162	1999 CW ₁₁₈
C76107.....	0.0	1999 Feb 10	40.298	41.190	0.6	22.65 \pm 0.07	6.55	278	1999 CB ₁₁₉
C76207.....	0.0	1999 Feb 10	43.531	44.415	0.6	22.97 \pm 0.06	6.54	280	1999 CC ₁₁₉
C76502.....	0.0	1999 Feb 10	44.301	45.161	0.6	23.56 \pm 0.14	7.06	220	1999 CD ₁₁₉
C76609.....	0.0	1999 Feb 10	44.002	44.852	0.6	24.11 \pm 0.11	7.64	169	1999 CX ₁₁₈
C76800.....	0.0	1999 Feb 10	28.873	29.711	1.0	23.19 \pm 0.04	8.52	112	1999 CE ₁₁₉
C76907.....	0.0	1999 Feb 10	42.953	43.778	0.7	23.96 \pm 0.08	7.59	172	1999 CW ₁₃₁
C79710.....	+0.5	1999 Feb 10	23.35 \pm 0.14	Lost
C79900.....	+0.5	1999 Feb 10	22.78 \pm 0.12	Lost
C85003.....	+0.5	1999 Feb 11	23.68 \pm 0.13	Lost
C85110.....	+0.5	1999 Feb 11	38.774	39.705	0.5	22.75 \pm 0.20	6.82	246	1999 CF ₁₁₉
C85200.....	+0.5	1999 Feb 11	41.806	42.739	0.4	23.63 \pm 0.07	7.37	191	1999 CG ₁₁₉
C85204.....	+0.5	1999 Feb 11	32.938	33.875	0.5	21.85 \pm 0.09	6.61	271	1999 CL ₁₅₈
C85300.....	+0.5	1999 Feb 11	45.906	46.845	0.4	23.88 \pm 0.23	7.22	204	1999 CH ₁₁₉
C85404.....	+0.5	1999 Feb 11	42.175	43.122	0.4	23.98 \pm 0.08	7.68	165	1999 CS ₁₅₃
C85410.....	+0.5	1999 Feb 11	23.82 \pm 0.08	Lost
C85504.....	+0.5	1999 Feb 11	41.130	42.082	0.4	24.24 \pm 0.16	8.05	139	1999 CK ₁₁₉
C85509.....	+0.5	1999 Feb 11	41.450	42.400	0.4	23.03 \pm 0.12	6.80	247	1999 CJ ₁₁₉
C85600.....	+0.5	1999 Feb 11	45.773	46.727	0.3	22.52 \pm 0.03	5.87	381	1999 CL ₁₁₉
C85700.....	+0.5	1999 Feb 11	41.159	42.117	0.3	23.25 \pm 0.10	7.05	220	1999 CM ₁₁₉
C85808.....	+0.5	1999 Feb 11	45.122	46.085	0.3	23.41 \pm 0.12	6.82	246	1999 CG ₁₅₄
C85904.....	+0.5	1999 Feb 11	43.697	44.664	0.3	23.96 \pm 0.24	7.51	179	1999 CN ₁₁₉
C85907.....	+0.5	1999 Feb 11	42.168	43.135	0.3	22.96 \pm 0.10	6.66	264	1999 CX ₁₃₁
C85909.....	+0.5	1999 Feb 11	23.99 \pm 0.05	Lost
C88505.....	0.0	1999 Feb 11	40.502	41.482	0.2	23.11 \pm 0.21	6.98	228	1999 CM ₁₅₃
C88600.....	0.0	1999 Feb 11	37.016	37.995	0.2	23.61 \pm 0.07	7.87	151	1999 CY ₁₃₁
C88608.....	0.0	1999 Feb 11	23.64 \pm 0.33	Lost
C88902.....	0.0	1999 Feb 11	41.998	42.968	0.2	23.99 \pm 0.08	7.71	163	1999 CZ ₁₃₁
C88905.....	0.0	1999 Feb 11	24.20 \pm 0.28	Lost
C89000.....	0.0	1999 Feb 11	42.306	43.273	0.3	23.75 \pm 0.14	7.44	185	1999 CN ₁₅₃
C89301.....	0.0	1999 Feb 11	38.704	39.660	0.4	22.91 \pm 0.26	6.97	229	1999 CA ₁₃₂
C89500.....	0.0	1999 Feb 11	43.383	44.330	0.4	23.99 \pm 0.04	7.57	173	1999 CQ ₁₅₃
C89503 ^d	0.0	1999 Feb 11	44.241	45.187	0.4	23.24 \pm 0.11	6.73	256	1995 DC ₀₂
C89507.....	0.0	1999 Feb 11	30.805	31.752	0.5	22.11 \pm 0.09	7.15	211	1999 CP ₁₃₃
C92411.....	-0.5	1999 Feb 11	27.797	28.719	0.7	21.89 \pm 0.22	7.38	190	1999 CM ₁₅₈
C98602.....	-0.5	1999 Feb 12	43.113	44.031	0.5	22.96 \pm 0.10	6.57	276	1999 CQ ₁₃₃
C98603.....	-0.5	1999 Feb 12	39.970	40.889	0.5	22.95 \pm 0.17	6.88	239	1999 CO ₁₅₃
C98703.....	-0.5	1999 Feb 12	41.324	42.250	0.5	23.85 \pm 0.14	7.64	168	1999 CR ₁₃₃
C99411.....	-0.5	1999 Feb 12	41.457	42.418	0.3	23.19 \pm 0.18	6.97	229	1999 CU ₁₅₃
C99502.....	-0.5	1999 Feb 12	42.006	42.970	0.3	23.73 \pm 0.25	7.45	184	1999 CH ₁₅₄
C04700.....	0	1999 Sep 6	42.054	42.964	0.6	23.83 \pm 0.25	7.54	176	1999 RS ₂₁₄
C04707.....	0	1999 Sep 6	39.838	40.754	0.6	23.49 \pm 0.14	7.45	184	1999 RT ₂₁₄
C04910.....	0	1999 Sep 6	44.240	45.167	0.5	22.96 \pm 0.23	6.45	291	1999 RU ₂₁₄
C05105.....	0	1999 Sep 6	47.685	48.626	0.4	24.08 \pm 0.20	7.26	201	1999 RV ₂₁₄
C09804.....	0	1999 Sep 6	41.990	42.944	0.4	23.47 \pm 0.34	7.19	207	1999 RW ₂₁₄
C10300.....	0	1999 Sep 6	44.694	45.621	0.5	22.90 \pm 0.20	6.36	304	1999 RX ₂₁₄
C10801.....	+10	1999 Sep 6	36.884	37.776	0.7	22.76 \pm 0.08	7.03	223	1999 RY ₂₁₄
C10908.....	+10	1999 Sep 6	39.016	39.906	0.7	23.42 \pm 0.10	7.46	183	1999 RZ ₂₁₄
C13601.....	0	1999 Sep 6	30.686	31.610	0.7	23.71 \pm 0.22	8.78	99	1999 RB ₂₁₅
C13604.....	0	1999 Sep 6	42.465	43.380	0.5	22.88 \pm 0.15	6.55	279	1999 RC ₂₁₅
C14209.....	+10	1999 Sep 6	37.824	38.692	0.8	23.08 \pm 0.11	7.24	202	1999 RD ₂₁₅
C18604.....	0	1999 Sep 7	41.618	42.588	0.4	22.57 \pm 0.17	6.32	309	1999 RE ₂₁₅
C18606.....	0	1999 Sep 7	43.000	43.964	0.4	22.95 \pm 0.07	6.57	276	1999 RF ₂₁₅
C21502.....	0	1999 Sep 7	44.015	45.017	0.2	23.49 \pm 0.13	6.98	228	1999 RG ₂₁₅
C21903.....	+10	1999 Sep 7	36.161	37.154	0.3	23.91 \pm 0.21	8.27	126	1999 RH ₂₁₅
C22100.....	+10	1999 Sep 7	34.047	35.041	0.3	22.42 \pm 0.08	7.03	223	1999 RJ ₂₁₅

TABLE 5—Continued

ID	β (deg)	Date	R (AU)	Δ (AU)	α' (deg)	$m_R \pm \sigma^a$	$m_R(1, 1, 0)^b$	D^c (km)	MPC Name
C24402	-10	1999 Sep 7	42.041	42.952	0.6	23.33 ± 0.11	7.04	222	1999 RK ₂₁₅
C24411	-10	1999 Sep 7	43.966	44.869	0.6	23.02 ± 0.11	6.56	277	1999 RN ₂₁₅
C24809	0	1999 Sep 7	39.498	40.391	0.7	23.93 ± 0.07	7.91	148	1999 RR ₂₁₅
C24902	0	1999 Sep 7	42.205	43.089	0.6	23.12 ± 0.19	6.83	245	1999 RT ₂₁₅
C25004	0	1999 Sep 7	39.515	40.383	0.7	22.87 ± 0.20	6.82	245	1999 RU ₂₁₅
C25101	+10	1999 Sep 7	35.622	36.466	0.9	23.73 ± 0.19	8.16	132	1999 RV ₂₁₅
C25103	+10	1999 Sep 7	32.291	33.139	1.0	23.31 ± 0.16	8.17	132	1999 RW ₂₁₅
C37507	-0.5	1999 Sep 8	41.130	42.059	0.5	23.42 ± 0.16	7.23	203	1999 RX ₂₁₅
C37701	-0.5	1999 Sep 8	36.314	37.262	0.5	22.25 ± 0.12	6.60	272	1999 RY ₂₁₅
C37703	-0.5	1999 Sep 8	39.955	40.905	0.5	22.04 ± 0.12	5.97	364	1999 RZ ₂₅₃
C38006	-10	1999 Sep 8	30.068	30.976	0.8	22.24 ± 0.16	7.40	188	1999 RZ ₂₁₅
C41409	+0.5	1999 Sep 8	42.379	43.377	0.2	23.08 ± 0.17	6.74	255	1999 RA ₂₁₆
C41607	+0.5	1999 Sep 8	33.725	34.718	0.3	22.42 ± 0.11	7.05	221	1999 RB ₂₁₆
C41611	+0.5	1999 Sep 8	46.992	47.985	0.2	23.56 ± 0.11	6.79	249	1999 RC ₂₁₆
D17405	0.0	2000 Mar 31	37.749	38.722	0.3	23.33 ± 0.16	7.51	179	2000 FX ₅₃
D30611 ^d	0.0	2000 Apr 2	41.298	42.278	0.3	23.39 ± 0.10	7.18	208	1994 GV ₉
D30711	0.0	2000 Apr 2	33.551	34.532	0.3	23.56 ± 0.12	8.24	127	2000 GK ₁₄₇
D45503	+20	2000 Apr 3	37.051	37.976	0.6	22.52 ± 0.20	6.78	250	2000 GM ₁₄₇
D45809	0.0	2000 Apr 3	40.209	41.205	0.1	23.81 ± 0.15	7.71	163	2000 GW ₁₄₆
D45904	0.0	2000 Apr 3	43.753	44.750	0.1	23.85 ± 0.11	7.40	188	2000 GY ₁₄₆
D45906	0.0	2000 Apr 3	43.605	44.602	0.1	23.18 ± 0.11	6.74	255	2000 GX ₁₄₆
D49511	0.0	2000 Apr 3	42.935	43.878	0.4	23.36 ± 0.15	6.99	228	2000 GZ ₁₄₆

NOTE.—Some quantities were not computed for lost objects because observations span only 2 hr.

^a Red magnitude of the object, with 1 σ error.

^b Absolute red magnitude at geocentric distance $\Delta = 1$ AU, heliocentric distance $R = 1$ AU, and phase angle $\alpha' = 0$, computed from discovery geometry.

^c Diameter D is computed directly from $m_R(1, 1, 0)$ via eq. (4), assuming $p_R \equiv 0.04$.

^d Previously known object serendipitously imaged in survey fields.

observable constraining $i_{1/2}$ is the inclination distribution and the observable constraining q is the absolute magnitude distribution. However, $N_{\text{CKBO}}(D > 100 \text{ km})$ is a function of both q and $i_{1/2}$ as a steeper size distribution or thicker

inclination distribution will each allow more bodies to be present. In the maximum likelihood simulations that follow, the ideal case would be to constrain q , $i_{1/2}$ and $N_{\text{CKBO}}(D > 100 \text{ km})$ and estimate errors in one simulation; however, this is difficult computationally. Therefore, we find the best-fit values of the three parameters in a single simulation but estimate the errors on the parameters in two simulations, one that estimates the q - $N_{\text{CKBO}}(D > 100 \text{ km})$ joint errors and one that estimates the $i_{1/2}$ - $N_{\text{CKBO}}(D > 100 \text{ km})$ joint errors. We then combine the two simulation results in quadrature to determine the errors on $N_{\text{CKBO}}(D > 100 \text{ km})$.

3. SIZE DISTRIBUTION OF THE CLASSICAL KBOS

We estimate the size distribution of the KBOS from our data in two ways. The first is a simple estimate made directly from the distribution of ecliptic KBO apparent magnitudes (CLF). The second is a model that simulates the discovery characteristics of our survey through the use of a maximum likelihood model constrained by the absolute magnitude of the classical KBOS.

3.1. Cumulative Luminosity Function

We model the CLF with a power-law relation, $\log \Sigma = \alpha(m_R - m_0)$ (§ 1). The KBOS are assumed to follow a differential power-law size distribution of the form $n(r)dr \propto r^{-q} dr$, where $n(r)dr$ is the number of objects having radii between r and $r + dr$ and q is the index of the size distribution. Assuming albedo and heliocentric distance distributions that are independent of KBO size, the simple transformation between the slope of the CLF (α) and the exponent of the size distribution (q) is given by

$$q = 5\alpha + 1 \quad (3)$$

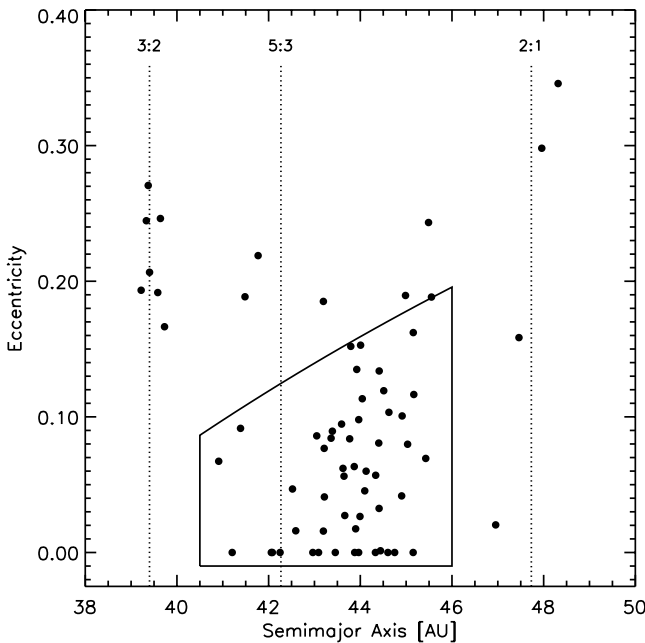


FIG. 6.—Eccentricity vs. semimajor axis of all KBOs discovered in this work with semimajor axes $a < 50$ AU. Note that few objects were found in the 3:2 resonance compared with previous studies. The area enclosed by a solid line indicates our criteria for selecting classical KBOS, semimajor axes $40.5 \text{ AU} < a < 46 \text{ AU}$ and perihelia $q' > 37 \text{ AU}$.

TABLE 6
CFHT ORBITAL ELEMENTS

ID	a (AU)	e	i (deg)	Ω (deg)	ω (deg)	M (deg)	MJD	Δt	MPC Name	Sim. ^a
C17000.....	54.81897	0.29808	18.754	336.974	98.551	29.501	51,800	2	1999 CC ₁₅₈	
C71710.....	44.00641	0.15285	25.441	119.004	137.939	236.881	51,800	2	1999 CD ₁₅₈	<i>i, q</i>
C72105.....	52.82586	0.28892	5.467	305.621	148.820	16.449	51,600	2	1999 CV ₁₁₈	
C72505.....	45.15557	0.16213	3.038	122.823	247.176	100.913	51,600	2	1999 CP ₁₅₃	<i>i, q</i>
C72600.....	40.91130	0.06725	17.068	127.720	322.119	35.433	51,800	2	1999 CK ₁₅₈	<i>i, q</i>
C75803.....	89.81583	0.61493	25.619	163.125	15.456	357.553	51,600	2	1999 CY ₁₁₈	
C75905.....	110.36855	0.65629	27.804	345.177	235.542	350.265	51,600	2	1999 CZ ₁₁₈	
C76103.....	45.15314	0.0	0.283	24.858	319.882	181.758	51,260	(86)	1999 CA ₁₁₉	<i>i, q</i>
C76104.....	43.45475	0.0	0.819	154.471	173.481	198.705	51,260	(86)	1999 CW ₁₁₈	<i>i, q</i>
C76107.....	43.64467	0.05625	9.160	168.036	358.276	0.071	51,240	(62)	1999 CB ₁₁₉	<i>i, q</i>
C76207.....	44.44015	0.00127	0.458	190.261	272.993	65.792	51,800	2	1999 CC ₁₁₉	<i>i, q</i>
C76502.....	43.99328	0.02655	2.396	166.381	183.867	180.075	51,240	(62)	1999 CD ₁₁₉	<i>i, q</i>
C76609.....	43.66175	0.02725	1.784	175.714	175.748	180.064	51,240	(62)	1999 CX ₁₁₈	<i>i, q</i>
C76800.....	39.33216	0.24461	1.429	171.557	1.040	0.083	51,240	(58)	1999 CE ₁₁₉	
C76907.....	43.19444	0.01577	7.952	174.627	209.869	150.003	51,600	2	1999 CF ₁₃₁	<i>i, q</i>
C85110.....	91.70394	0.58203	19.700	303.437	203.636	354.915	51,600	2	1999 CG ₁₁₉	
C85200.....	51.35701	0.33914	16.656	304.264	257.457	317.562	51,600	2	1999 CG ₁₁₉	
C85204.....	41.77052	0.21889	10.025	120.074	325.711	26.075	51,800	2	1999 CL ₁₅₈	
C85300.....	43.39088	0.08942	19.968	122.349	156.415	210.747	51,600	2	1999 CH ₁₁₉	<i>i, q</i>
C85404.....	44.51143	0.11926	0.983	343.336	223.233	293.035	51,600	2	1999 CS ₁₅₃	<i>i, q</i>
C85504.....	42.08155	0.0	11.592	123.077	2.999	0.000	51,220	(8)	1999 CK ₁₁₉	<i>i, q</i>
C85509.....	45.42766	0.06934	3.200	313.350	189.726	346.285	51,600	2	1999 CJ ₁₁₉	<i>i, q</i>
C85600.....	46.95343	0.02034	23.292	125.157	284.096	76.274	51,600	2	1999 CL ₁₁₉	
C85700.....	44.41239	0.13382	2.744	118.490	294.453	61.472	51,600	2	1999 CM ₁₁₉	<i>i, q</i>
C85808.....	43.04996	0.08599	0.766	100.205	176.323	219.095	51,600	2	1999 CG ₁₅₄	<i>i, q</i>
C85904.....	43.89874	0.01744	0.997	347.227	323.092	180.915	51,600	2	1999 CN ₁₁₉	<i>i, q</i>
C85907.....	41.48466	0.18854	9.760	127.984	114.269	269.788	51,600	2	1999 CX ₁₃₁	
C88505.....	44.12661	0.05994	0.190	87.878	60.139	0.067	51,240	(57)	1999 CM ₁₅₃	<i>i, q</i>
C88600.....	43.92279	0.13496	25.167	148.245	0.110	359.999	51,220	(8)	1999 CY ₁₃₁	<i>i, q</i>
C88902.....	44.41005	0.03248	2.371	151.799	359.878	359.999	51,220	(8)	1999 CZ ₁₃₁	<i>i, q</i>
C89000.....	42.59212	0.01599	7.480	153.050	179.417	180.056	51,240	(56)	1999 CN ₁₅₃	<i>i, q</i>
C89301.....	43.96574	0.09794	12.071	154.871	0.530	0.067	51,240	(56)	1999 CA ₁₃₂	<i>i, q</i>
C89500.....	44.33005	0.0	0.208	181.177	336.136	0.000	51,220	(30)	1999 CQ ₁₅₃	<i>i, q</i>
C89503 ^b	43.86806	0.06335	2.349	154.182	124.958	244.781	51,200	5	1995 DC ₀₂	<i>i, q</i>
C89507.....	39.21917	0.19335	2.946	333.980	171.178	8.172	51,240	(63)	1999 CP ₁₃₃	
C92411.....	39.37318	0.27060	9.242	338.951	182.862	0.078	51,240	(60)	1999 CM ₁₅₈	
C98602.....	41.38725	0.09152	13.265	123.288	220.788	131.912	51,600	2	1999 CQ ₁₃₃	<i>i, q</i>
C98603.....	43.76827	0.08381	0.805	278.110	162.704	36.595	51,600	2	1999 CO ₁₅₃	<i>i, q</i>
C98703.....	42.24989	0.0	1.727	135.130	347.987	0.000	51,220	(6)	1999 CR ₁₃₃	<i>i, q</i>
C99411.....	44.09712	0.04544	2.698	139.275	25.598	329.621	51,600	2	1999 CU ₁₅₃	<i>i, q</i>
C99502.....	43.36260	0.08425	0.843	164.676	54.980	282.282	51,600	2	1999 CH ₁₅₄	<i>i, q</i>
C04700.....	42.96436	0.0	3.174	139.496	178.818	0.000	51,440	(33)	1999 RS ₂₁₄	<i>i, q</i>
C04707.....	42.52058	0.04681	2.578	138.065	151.541	27.528	51,800	2	1999 RT ₂₁₄	<i>i, q</i>
C04910.....	95.52823	0.68200	4.169	137.804	261.582	345.449	51,460	(68)	1999 RU ₂₁₄	
C05105.....	45.03200	0.07981	1.149	144.629	357.831	180.129	51,440	(34)	1999 RV ₂₁₄	<i>i, q</i>
C09804.....	43.21204	0.07676	1.370	0.376	90.714	280.315	51,800	2	1999 RW ₂₁₄	<i>i, q</i>
C10300.....	44.90203	0.04172	4.818	3.793	247.094	111.571	51,800	2	1999 RX ₂₁₄	<i>i, q</i>
C10801.....	45.55261	0.18833	13.689	327.338	72.154	340.779	51,800	2	1999 RY ₂₁₄	
C10908.....	87.18745	0.57385	20.301	214.776	117.659	8.376	51,460	(65)	1999 RZ ₂₁₄	
C13601.....	48.31520	0.34575	7.814	4.997	1.548	0.096	51,460	(66)	1999 RB ₂₁₅	
C13604.....	44.33566	0.05693	1.399	189.037	249.705	295.722	51,800	2	1999 RC ₂₁₅	<i>i, q</i>
C14209.....	120.78728	0.68630	25.884	210.337	141.064	2.795	51,800	2	1999 RD ₂₁₅	
C18604.....	45.16729	0.11648	1.344	149.278	112.725	55.573	51,800	2	1999 RE ₂₁₅	<i>i, q</i>
C18606.....	43.96413	0.0	3.675	327.579	0.196	0.000	51,460	(65)	1999 RF ₂₁₅	<i>i, q</i>
C21502.....	47.46151	0.15843	0.252	294.642	122.868	298.384	51,800	2	1999 RG ₂₁₅	
C21903.....	43.79253	0.15198	10.212	276.873	68.428	357.760	51,800	2	1999 RH ₂₁₅	<i>i</i>
C22100.....	59.78767	0.42018	19.719	314.937	43.698	355.025	51,800	2	1999 RJ ₂₁₅	
C24402.....	39.72913	0.16644	11.499	137.761	103.443	110.966	51,460	(65)	1999 RK ₂₁₅	
C24411.....	43.21648	0.04096	12.404	140.634	68.292	159.483	51,800	2	1999 RN ₂₁₅	<i>i</i>
C24809.....	44.91243	0.10067	1.144	185.694	185.986	0.104	51,460	(65)	1999 RR ₂₁₅	<i>i, q</i>
C24902.....	43.08942	0.0	21.907	192.898	179.849	0.000	51,460	(63)	1999 RT ₂₁₅	<i>i, q</i>
C25004.....	43.59152	0.09467	7.718	14.298	316.918	36.841	51,800	2	1999 RU ₂₁₅	<i>i, q</i>
C25101.....	44.98636	0.18949	21.975	351.818	27.099	359.849	51,800	2	1999 RV ₂₁₅	
C25103.....	39.63957	0.24625	10.424	253.992	180.867	322.404	51,460	(63)	1999 RW ₂₁₅	
C37507.....	42.05898	0.0	0.894	99.349	223.581	0.000	51,440	(32)	1999 RX ₂₁₅	<i>i, q</i>

TABLE 6—Continued

ID	a (AU)	e	i (deg)	Ω (deg)	ω (deg)	M (deg)	MJD	Δt	MPC Name	Sim. ^a
C37701	45.48866	0.24329	22.180	326.622	51.565	328.531	51,800	2	1999 RY ₂₁₅	
C37703	44.04333	0.11336	0.563	84.582	297.742	315.250	51,800	2	1999 RZ ₂₅₃	<i>i, q</i>
C38006	102.15245	0.69681	25.492	341.669	336.567	0.548	51,800	2	1999 RZ ₂₁₅	
C41409	44.62426	0.10334	0.787	192.150	80.444	69.830	51,800	2	1999 RA ₂₁₆	<i>i, q</i>
C41607	47.95883	0.29806	12.669	175.730	208.315	345.437	51,800	2	1999 RB ₂₁₆	
C41611	44.40277	0.08068	0.588	190.538	344.286	180.149	51,460	(62)	1999 RC ₂₁₆	<i>i, q</i>
D17405	43.19458	0.18511	4.799	175.196	68.292	312.820	51,640	(37)	2000 FX ₅₃	
D30611 ^b	43.62227	0.06202	0.565	176.852	301.264	57.670	51,800	7	1994 GV ₉	<i>i, q</i>
D30711	39.40243	0.20660	7.164	1.681	243.983	316.246	51,640	(35)	2000 GK ₁₄₇	
D45503	39.58196	0.19165	18.077	96.123	173.826	292.969	51,640	(33)	2000 GM ₁₄₇	
D45809	41.20546	0.00000	28.975	8.913	179.957	0.000	51,620	(1)	2000 GW ₁₄₆	<i>i, q</i>
D45904	44.74976	0.0	2.718	13.462	134.077	42.017	51,640	(34)	2000 GY ₁₄₆	<i>i, q</i>
D45906	44.60190	0.0	0.664	344.290	204.949	0.066	51,640	(34)	2000 GX ₁₄₆	<i>i, q</i>
D49511	43.87783	0.00000	1.999	215.697	357.395	0.000	51,620	(2)	2000 GZ ₁₄₆	<i>i, q</i>

NOTE.—Orbits of all objects discovered, excluding the seven lost objects that had insufficient time bases (2 hr) to provide meaningful orbits. The Keplerian orbital elements a , e , i , Ω , ω , and M represent semimajor axis, eccentricity, inclination, longitude of ascending node, argument of perihelion, and mean anomaly, respectively. MJD is the Modified Julian Date of the orbit computation, and Δt is the time base in oppositions or days (in parentheses) if less than two oppositions. Orbital elements were computed independently by the Minor Planet Center and by D. Tholen (University of Hawaii).

^a Simulation in which the object was used: q and/or i . All CKBOs were used in the i simulation, and all CKBOs discovered in ecliptic fields were used in the q simulation.

^b This known object was serendipitously imaged in survey fields.

(Irwin et al. 1995). Under these assumptions, the size distribution can be estimated directly from the CLF.

We estimated the CLF by multiplying the detection statistics from the observed distribution of object brightnesses by the inverse of the detection efficiency. We assumed Poisson detection statistics, with error bars indicating the interval over which the integrated Poisson probability distribution for the observed number of objects contains 68.27% of the total probability (identical to the errors derived by Kraft, Burrows, & Nousek 1991). This is nearly equal to the Gaussian case for all data points resulting from more than a few detections. We have included all 74 KBOs discovered in our 37.2 deg² of ecliptic fields in the estimate of the CLF. This includes the lost objects, as the CLF is simply a count of the number of bodies discovered at a given apparent magnitude. Our results appear in Figure 7, with other published KBO surveys. All observations were converted to R band if necessary assuming $V - R = 0.5$ for KBOs (Luu & Jewitt 1996), and error bars were computed assuming Poisson detection statistics. The data point of Cochran et al. (1995) near $m_R = 28$ was omitted because of major uncertainties about its reliability (Brown, Kulkarni, & Liggett 1997; cf. Cochran et al. 1998). Early photographic plate surveys (Tombaugh 1961, portions of Luu & Jewitt 1988, and Kowal 1989) have unproved reliability at detecting faint slow-moving objects, and plate emulsion variations and defects make accurate photometric calibration difficult. The photographic plate survey data were not used in our analysis.

The CLF points are highly correlated with one another, resulting in a heavy weighting of the bright object data points. Thus, we fitted the differential luminosity function (DLF) instead. We plot the DLF data points at the faint end of the bin, representing the modal value in that bin. Very small bin sizes were chosen (0.1 mag) to negate binning effects incurred from averaging the detection efficiency (eq. [2]) over a large magnitude range. For any nonzero CLF slope, α , the DLF and CLF slopes are equal due to the

exponential nature of the CLF. The DLF was modeled by evaluating the Poisson probability of detecting the observed DLF given a range of m_0 and α , with the maximum probability corresponding to our best-fit values. Error bars were determined by finding the contours of constant joint probability for m_0 and α enclosing 68.27% of the total probability, a procedure similar to that used below for the maximum likelihood simulation. Computations from this procedure are summarized in Table 7. We find that the slope of the CLF is $\alpha = 0.64^{+0.11}_{-0.10}$ with $m_0 = 23.23^{+0.15}_{-0.20}$, which corresponds to $q = 4.2 \pm 0.5$ from equation (3). We also fitted the CLF by applying the maximum likelihood method described by Gladman et al. (1998) to our data, which yields statistically identical results to the binned DLF procedure: $\alpha = 0.63 \pm 0.06$ and $m_0 = 23.04^{+0.08}_{-0.09}$, corresponding to $q = 4.2 \pm 0.3$. The maximum likelihood method provides slightly better signal-to-noise ratio and is independent of binning effects. We adopt the maximum likelihood procedure as our formal estimate of the CLF slope. Both methods estimating the size distribution are in statistical agreement with the more detailed analysis presented in the next section.

The best-fit $\alpha = 0.63$ mag distribution was compared with the observed magnitude distribution using a Kolmogorov-Smirnov test (Press et al. 1992), producing a value of $D = 0.13$. If the model and the data distributions were identical, a deviation greater than this would occur by chance 12% of the time. Thus, our linear model is not a perfect fit, but it is statistically acceptable.

3.2. Maximum Likelihood Simulation

We now present more detailed analysis of the size distribution. Since we model the detection statistics of an assumed population, we choose to model the 49 classical KBOs discovered on the ecliptic as they are numerically dominant in the observations and their orbital parameters are more easily modeled than other KBO classes. Our selection criteria for CKBOs are perihelion $q' > 37$ AU and 40.5

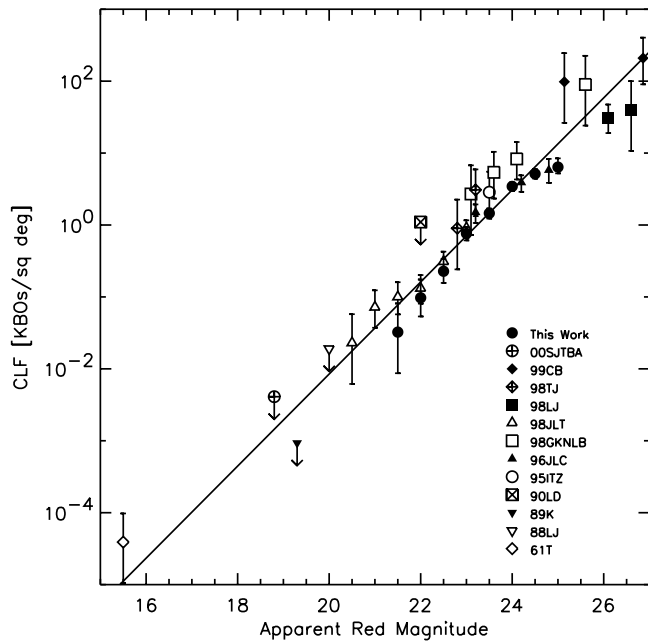


FIG. 7.—Our measurement of the cumulative luminosity function (CLF), which represents the number of KBOs per square degree near the ecliptic (*filled circles*) brighter than a given apparent red magnitude. Other points are previous works, with arrows denoting upper limits. The line represents a fit to our data alone, yielding $\alpha = 0.63 \pm 0.06$, corresponding to $q = 4.12 \pm 0.3$ assuming the albedo and heliocentric distance distributions are independent of the size distribution. Abbreviations are as follows: 00SJTB is Sheppard et al. (2000), 99CB is Chiang & Brown (1999), 98GKNLB is Gladman et al. (1998), 98JLT is Jewitt, Luu, & Trujillo (1998), 98LJ is Luu & Jewitt (1998), 98TJ is Trujillo & Jewitt (1998), 96JLC is Jewitt, Luu, & Chen (1996), 95ITZ is Irwin, Tremaine & Żytkow (1995), 90LD is Levison & Duncan (1990), 89K is Kowal (1989), 88LJ is Luu & Jewitt (1988), and 61T is Tombaugh (1961).

$\text{AU} < a < 46 \text{ AU}$. Given the size of an object and its orbital parameters, we can compute its position, velocity, and brightness, allowing a full Monte Carlo style analysis of the bias effects of our data collection procedures. The apparent

brightness was computed from

$$m = m_{\odot} - 2.5 \log [p_R \Phi(\alpha') r^2] + 2.5 \log (2.25 \times 10^{16} R^2 \Delta^2), \quad (4)$$

where α' is the phase angle of the object, $\Phi(\alpha')$ is the Bowell et al. (1989) phase function, geometric red albedo is given by p_R , r is the object radius in kilometers, R is the heliocentric distance, and Δ is the geocentric distance, both in AU (Jewitt & Luu 1995). The apparent red magnitude of the Sun was taken to be $m_{\odot} = -27.1$. For this work, we assume $p_R = 0.04$, consistent with a dark Centaur-like albedo (Jewitt & Luu 2000). We neglect phase effects [setting $\Phi(\alpha') \equiv 1$], since the maximum phase angle of an object at $R = 40 \text{ AU}$ within 1.5 hr of opposition is $\alpha' = 0^{\circ}.55$. This corresponds to $\Phi(\alpha') = 0.91$, a change in brightness of only 0.09 mag, which is less than other uncertainties in the data.

The apparent brightness is used in a biasing correction procedure (Trujillo et al. 2000; Trujillo 2000), summarized here:

1. A model distribution of KBOs is assumed (described in Table 8).
2. KBOs are drawn randomly from the model distribution.
3. For each KBO, the apparent speed and ecliptic coordinates are computed from the equations of Sykes & Moynihan (1996; a sign error was found in eq. [2] of their text and corrected), and compared with the observed fields and speed criteria.
4. The apparent magnitude is computed from equation (4).
5. The efficiency function (eq. [2]) and our field area covered are used to determine whether the simulated object would be “detected” in our survey.
6. A histogram of the detection statistics for the simulated objects is constructed, logarithmically binned by object size for the size distribution model and binned by inclination for the inclination distribution model. Binning effects were negligible because of small bin choice.
7. Steps 1–6 are repeated until the number of detected simulated objects is at least a factor 10 greater than the

TABLE 7
CLF AND DLF COMPUTATION

m_R Range ^a	$N'_{\text{DLF}}{}^b$	$N'_{\text{CLF}}{}^c$	$\bar{\epsilon}^d$	$N_{\text{DLF}}{}^e$	$N_{\text{CLF}}{}^f$	$\Sigma_{\text{DLF}}{}^g$	$\Sigma_{\text{CLF}}{}^h$
21.0–21.5.....	1	1	0.83	1.2	1.2	$0.03^{+0.05}_{-0.02}$	$0.03^{+0.05}_{-0.02}$
21.5–22.0.....	2	3	0.83	2.4	3.6	$0.06^{+0.06}_{-0.04}$	$0.10^{+0.08}_{-0.04}$
22.0–22.5.....	4	7	0.83	4.8	8.5	$0.13^{+0.08}_{-0.06}$	$0.23^{+0.11}_{-0.07}$
22.5–23.0.....	16	23	0.80	19.9	28.4	$0.54^{+0.13}_{-0.13}$	$0.76^{+0.17}_{-0.15}$
23.0–23.5.....	18	41	0.70	25.9	54.2	$0.70^{+0.16}_{-0.16}$	$1.46^{+0.24}_{-0.22}$
23.5–24.0.....	25	66	0.34	73.8	128.1	$1.98^{+0.40}_{-0.40}$	$3.44^{+0.46}_{-0.46}$
24.0–24.5.....	7	73	0.11	63.3	191.4	$1.70^{+0.74}_{-0.57}$	$5.14^{+0.87}_{-0.73}$
24.5–25.0.....	1	74	0.02	46.2	237.5	$1.24^{+1.86}_{-0.91}$	$6.38^{+2.06}_{-1.17}$

^a Apparent red magnitude range.

^b Number of KBOs found within $0^{\circ}.5$ of the ecliptic in the m_R range.

^c Cumulative number of ecliptic KBOs found.

^d Mean efficiency correction ϵ for the given m_R range.

^e Bias-corrected number of KBOs, computed by summing $1/\epsilon$ (eq. [2]) for all objects in the magnitude range.

^f Cumulative bias-corrected number of KBOs.

^g Bias-corrected surface density for the given magnitude range, equal to N_{DLF}/A , where $A = 37.2 \text{ deg}^2$; errors are computed from 1σ Poisson errors for N_{DLF} .

^h Bias-corrected cumulative surface density; errors are summed in quadrature from the Σ_{DLF} errors.

TABLE 8
CLASSICAL KBO SIZE DISTRIBUTION MODEL PARAMETERS

Symbol	Value	Distribution	Description
a	40.5–46 AU	$n(a)da \sim a^{1-p} da$	Semimajor axis
p^a	2	...	Semimajor-axis power
e	0–0.25	Uniform	Eccentricity
q'	$q' > 37$ AU	...	Perihelion distance
i	0°–90°	Gaussian, $i_{1/2}$ half-width	Inclination distribution
$i_{1/2}$	20°	...	Half-width of the inclination distribution
ω	0°–360°	Uniform	Argument of perihelion
Ω	0°–360°	Uniform	Longitude of the ascending node
M	0°–360°	Uniform	Mean anomaly
r	50–1000 km	$n(r)dr \sim r^{-q} dr$	Radius
q	Fitted	...	Size distribution index
p_R	0.04	...	Geometric red albedo
$N_{\text{CKBO}}(D > 100 \text{ km})$	Fitted	...	Number of CKBOs with diameters > 100 km
...	20	...	Number of radius bins (logarithmic intervals)
...	50–1000 km	...	Radius bin range

^a In the circular-orbit case, p corresponds to the power of the decrease in ecliptic-plane surface density Σ_{ecl} as a function of heliocentric distance R , $\Sigma_{\text{ecl}} \sim R^{-p}$.

number of observed objects in each histogram bin (typically requiring a sample of $10^6 < N < 10^8$ simulated objects, depending on the observed distribution).

8. The likelihood of producing the observed population from the model is estimated by assuming that Poisson detection statistics [$P = (\mu^n/n!) \exp(-\mu)$] apply to each histogram bin, where μ represents the expected number of simulated objects “discovered” given the number of objects simulated and n represents the true number of KBOs observed. Thus, the observed size distribution, calculated from equation (4), is used to constrain the q -model, and the observed inclination distribution is used to constrain the i -model (§ 4).

These steps are repeated for each set of model parameters in order to estimate the likelihood of producing the observations for a variety of models.

For the size distribution analysis, we take our best-fit model of the width of the inclination distribution (half-width $i_{1/2} = 20^\circ$, as estimated in the next section) and vary the size distribution index q , and the total number of objects $N_{\text{CKBO}}(D > 100 \text{ km})$. Model parameters are summarized in Table 8 and results appear in Figure 8. Our best-fit values are

$$q = 4.0^{+0.6}_{-0.5} \text{ (1 } \sigma), \quad q = 4.0^{+1.3}_{-1.1} \text{ (3 } \sigma),$$

$$N_{\text{CKBOs}}(D > 100 \text{ km}) = 3.8^{+2.0}_{-1.5} \times 10^4 \text{ (1 } \sigma),$$

$$N_{\text{CKBOs}}(D > 100 \text{ km}) = 3.8^{+5.4}_{-2.7} \times 10^4 \text{ (3 } \sigma),$$

where the errors for $N_{\text{CKBO}}(D > 100 \text{ km})$ have been combined in quadrature from the results of the q and $i_{1/2}$ fits, as described at the end of § 2.1. The values for q are consistent with previously published works (Table 9) and the q derived from the CLF data in the simple model (eq. [3]). The results are consistent with the distribution of large ($D > 150 \text{ km}$) main-belt asteroids ($q = 4.0$; Cellino, Zappalà, & Farinella 1991) and rock crushed by hypervelocity impacts ($q = 3.4$; Dohnanyi 1969). In addition, the scenario where the cross-sectional area (and thus optical scattered light and thermal emission) is concentrated in the largest objects ($q < 3$; Dohnanyi 1969) is ruled out at the greater than 2σ ($> 95.4\%$ confidence) level. Our results are also consistent with Kenyon & Luu (1999), who simulate the growth and veloc-

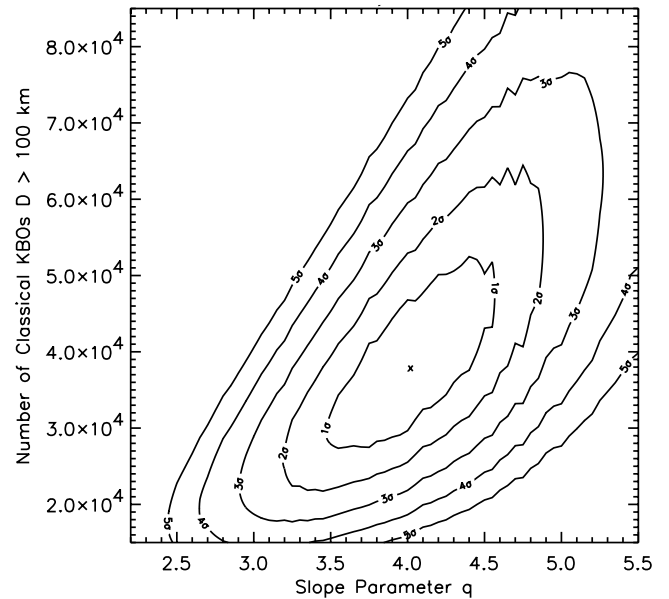


FIG. 8.—Maximum likelihood simulation of the size distribution power-law exponent. Contours of constant likelihood (1, 2, ..., 5 σ) are shown for a model with differential size distribution q (x-axis) and total number of objects greater than 100 km in diameter $N(D > 100 \text{ km})$ (y-axis). The maximum likelihood parameters (denoted by a cross) occur at $q = 4.0$ and $N_{\text{CKBO}}(D > 100 \text{ km}) = 3.8 \times 10^4$.

TABLE 9
SELECTED SIZE DISTRIBUTION MEASUREMENTS OF THE KBOs

m_R Range of Discovery	KBOs Found	q	Reference
21.1–24.6	86	$4.0^{+0.6}_{-0.5}$	This work
25.5–27.2 ^a	2	3.6 ± 0.1	Chiang & Brown 1999 ^b
23.8–26.7	6	3.7 ± 0.2	Luu & Jewitt 1998 ^b
23.0–25.8	5	$4.8^{+0.5}_{-0.6}$	Gladman et al. 1998 ^b
20.6–23.0	13	4.0 ± 0.5	Jewitt et al. 1998 ^b

^a V magnitude.

^b Calculated from CLF slope, α , via eq. (3).

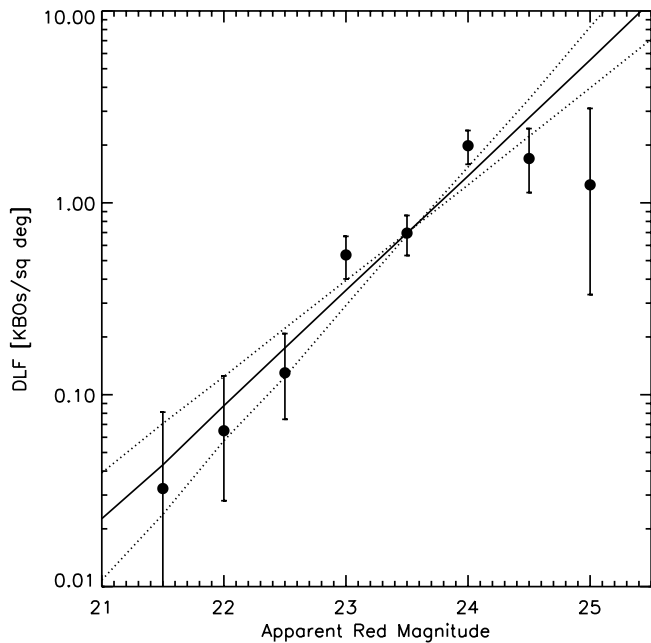


FIG. 9.—Differential luminosity function (DLF), equal to the number of KBOs per square degree near the ecliptic (filled circles). Three different models of the observed magnitude distribution are plotted from our maximum likelihood model, representing the expected DLF for the -1σ (dotted line), best-fit (solid line), and $+1\sigma$ (dotted line) cases of $q = 3.5, 4.0,$ and $4.6,$ respectively.

ity evolution of the Kuiper Belt during the formation era in the solar system. They find several plausible models for the resulting size distribution, all of which have $q \approx 4$.

In Figure 9, we plot the best-fit model CKBO distribution with the observed DLF to demonstrate the expected results from different size distributions. The magnitude distribution expected from the maximum likelihood model was compared with the observed magnitude distribution, as was done for the CLF-derived magnitude distribution in § 3.1. The Kolmogorov-Smirnov test produced $D = 0.17$; a greater deviation would occur by chance 11% of the time.

In our classical KBO maximum likelihood simulation, we have ignored possible contributions of the seven lost KBOs, since their orbital classes are not known. However, including them in the simulations by assuming circular orbits at the heliocentric distance of discovery results in statistically identical results for q , and the expected 7/49 rise in $N_{\text{CKBO}}(D > 100 \text{ km})$.

4. INCLINATION DISTRIBUTION OF THE CLASSICAL KBOs

The dynamical excitation of the Kuiper Belt is directly related to the inclination distribution of the KBOs. We present the inclinations of the CKBOs found in the CFHT survey in Figure 10. Assuming heliocentric observations, a KBO in circular orbit follows

$$\sin \beta = \sin i \sin f, \quad (5)$$

where β is the heliocentric ecliptic latitude, $0^\circ < i < 90^\circ$ is the inclination, and $0^\circ < f < 360^\circ$ represents the true anomaly of the object's orbit with $f = 0^\circ$ and 180° representing the ecliptic plane crossing (the longitude of perihelion is defined as 0 in this case). Using equation (5), we plot the fraction of each orbit spent at various ecliptic latitudes as a function of i (Fig. 11). This plot demonstrates two

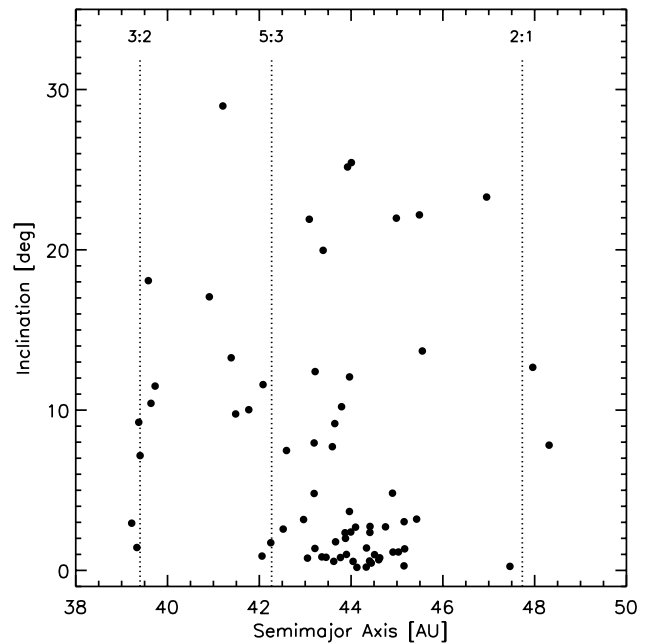


FIG. 10.—Inclination vs. semimajor axis of all KBOs discovered in this work with semimajor axes $a < 50 \text{ AU}$.

trends concerning the ecliptic latitude of observations β_{obs} . First, high-inclination objects are a factor 3–4 times more likely to be discovered when $\beta_{\text{obs}} \sim i$ than when observing at low ecliptic latitudes ($\beta_{\text{obs}} < i$). Second, the number of expected high-inclination objects drops precipitously, roughly as $1/i$, once $i > 1.5\beta_{\text{obs}}$ (Jewitt et al. 1996).

These facts led us to observe at three different ecliptic latitudes ($0^\circ, 10^\circ,$ and 20°) to better sample the high-inclination objects. During two observation periods (1999 September and 2000 March), care was made to interleave

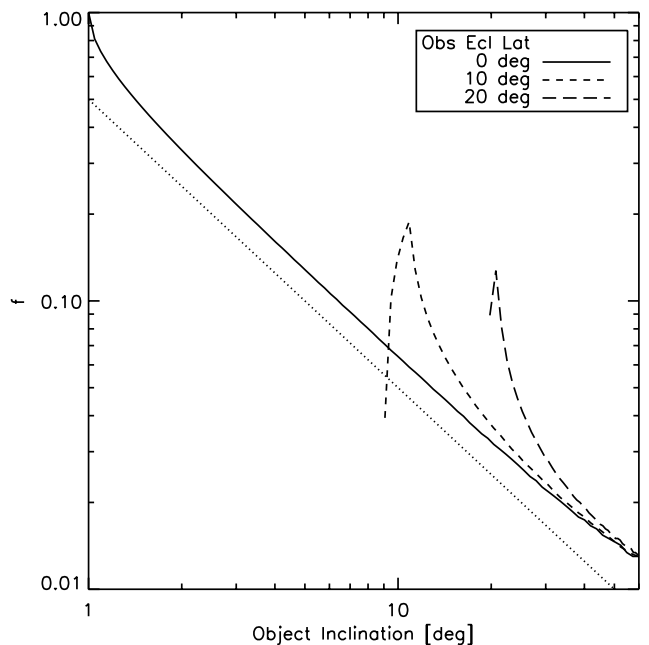


FIG. 11.—Fraction f of an orbit spent within $\pm 1^\circ$ (solid line), $10^\circ \pm 1^\circ$ (short-dashed line), and $20^\circ \pm 1^\circ$ (long-dashed line) of the ecliptic, as a function of object inclination i . The dotted line has a slope of $1/i$.

the ecliptic fields with the off-ecliptic fields on timescales of ~ 30 minutes. This technique provides immunity to drift in the limiting magnitude that might otherwise occur in response to typical slow changes in the seeing through the night. The results for the robust, interleaved fields matched those for the seeing-corrected 1999 February fields where fields were interleaved on much longer timescales of ~ 3 hr. Accordingly, we combined the data sets from all epochs to improve signal-to-noise ratio. In the next sections, we analyze the inclination distribution using two techniques to demonstrate the robustness of our method.

4.1. *Simple Inclination Model*

First, since fields were imaged at three different ecliptic latitudes, the surface density of objects at each latitude band [$\Sigma(0^\circ)$, $\Sigma(10^\circ)$, and $\Sigma(20^\circ)$] can directly yield the underlying inclination distribution. In our simple model, we generate an ensemble of inclined, circular orbits drawn from a Gaussian distribution centered on the ecliptic, and having a characteristic half-width of $i_{1/2}$. The probability of drawing a KBO with inclination between i and $i + di$ is given by

$$P(i)di = \frac{1}{\sigma\sqrt{2\pi}} \exp\left(\frac{-i^2}{2\sigma^2}\right)di, \quad (6)$$

where $\sigma = i_{1/2}(2 \ln 2)^{-1/2}$. Using this relation, and equation (5), we simulate the expected values of $\Sigma(0^\circ)$, $\Sigma(10^\circ)$, and $\Sigma(20^\circ)$ for various $i_{1/2}$. These are compared with two ratios measured from our observations, $R(10^\circ, 0^\circ) \equiv \Sigma(10^\circ)/\Sigma(0^\circ)$ and $R(20^\circ, 0^\circ) \equiv \Sigma(20^\circ)/\Sigma(0^\circ)$. Results appear in Table 10, and demonstrate that the characteristic half-width of the inclination distribution in the Kuiper Belt is $i_{1/2} \sim 17^{+10}_{-4}$ deg (1 $\sigma = 68.27\%$ confidence). This simple model does not use the observed inclination distribution of the individual objects, merely the surface density of objects found at each ecliptic latitude, and thus we have combined all objects from all KBO classes into this estimate.

4.2. *Full Maximum Likelihood Inclination Model*

Second, we use the maximum likelihood model described in § 3.1. We list the parameters of the model in Table 11. This model encompasses the additional constraint of the

TABLE 10
SIMPLE INCLINATION MODEL

Parameter	$\beta = 0^\circ$	$\beta = 10^\circ$ ^a	$\beta = 20^\circ$
Number of fields	119	94	19
Field area (deg ²)	37.2	29.8	6.0
Number of KBOs	74	11	1
Surface density (deg ⁻²) ^b	$1.80^{+0.22}_{-0.20}$	$0.34^{+0.12}_{-0.10}$	$0.17^{+0.25}_{-0.12}$
$R(10^\circ, 0^\circ)$ and $R(20^\circ, 0^\circ)$	$0.19^{+0.07}_{-0.06}$	$0.09^{+0.13}_{-0.07}$
$i_{1/2}$ (deg)	14^{+6}_{-3}	19^{+20}_{-7}

^a Results for ecliptic latitude $\beta = +10^\circ$ are consistent with those of $\beta = -10^\circ$ and so were combined.

^b Error bars were computed assuming Poisson detection statistics (Kraft et al. 1991).

observed inclination distribution, as well as the parallactic motion of Earth and KBO orbital motion to produce more realistic results. Results appear in Figure 12, with $N_{\text{CKBO}}(D > 100 \text{ km})$ representing the number of CKBOs with diameters greater than 100 km. The maximum likelihood occurs at

$$i_{1/2} = 20^{+6}_{-4} \text{ deg (1 } \sigma), \quad i_{1/2} = 20^{+26}_{-8} \text{ deg (3 } \sigma),$$

$$N_{\text{CKBOs}}(D > 100 \text{ km}) = 3.8^{+2.0}_{-1.5} \times 10^4 \text{ (1 } \sigma),$$

$$N_{\text{CKBOs}}(D > 100 \text{ km}) = 3.8^{+5.4}_{-2.7} \times 10^4 \text{ (3 } \sigma),$$

where the errors for $N_{\text{CKBO}}(D > 100 \text{ km})$ have been estimated from the $i_{1/2}$ and q fits, combined in quadrature, as described at the end of § 2.1. This maximum likelihood model is consistent with the simple model described in § 4.1. In Figure 13, we plot the observed surface density of objects as a function of ecliptic latitude and compare these data to our best-fit models. This illustrates the fundamental fact that even though the true inclination distribution of the KBOs is very thick ($i_{1/2} \approx 20^\circ$), the surface density drops off quickly with ecliptic latitude, reaching half the ecliptic value at an ecliptic latitude of $\beta \approx 3^\circ$ [$\Sigma(3^\circ)/\Sigma(0^\circ) < 0.5$].

The functional form of the inclination distribution cannot be well constrained by our data. However, the best-fit Gaussian distribution was compared to a flat-top (“top hat”) inclination distribution, with a uniform number of

TABLE 11
KBO INCLINATION MODEL PARAMETERS

Symbol	Value	Distribution	Description
a	40.5–46 AU	$n(a)da \sim a^{1-p} da$	Semimajor axis
p^a	2	...	Semimajor-axis power
e	0–0.25	Uniform	Eccentricity
q'	$q' > 37 \text{ AU}$...	Perihelion distance
i	0° – 90°	Gaussian, $i_{1/2}$ half-width	Inclination distribution
$i_{1/2}$	Fitted	...	Half-width of inclination distribution
ω	0° – 360°	Uniform	Argument of perihelion
Ω	0° – 360°	Uniform	Longitude of the ascending node
M	0° – 360°	Uniform	Mean anomaly
r	50–1000 km	$n(r)dr \sim r^{-q} dr$	Radius
q	4.0	...	Slope parameter
p_R	0.04	...	Red albedo
$N_{\text{KBO}}(D > 100 \text{ km})$	Fitted	...	Number of CKBOs with diameters $> 100 \text{ km}$
...	45	...	Number of inclination bins
...	0° – 90°	...	Inclination bin range

^a In the circular-orbit case, p corresponds to the power of the decrease in ecliptic-plane surface density Σ_{ecl} as a function of heliocentric distance R , $\Sigma_{\text{ecl}} \sim R^{-p}$.

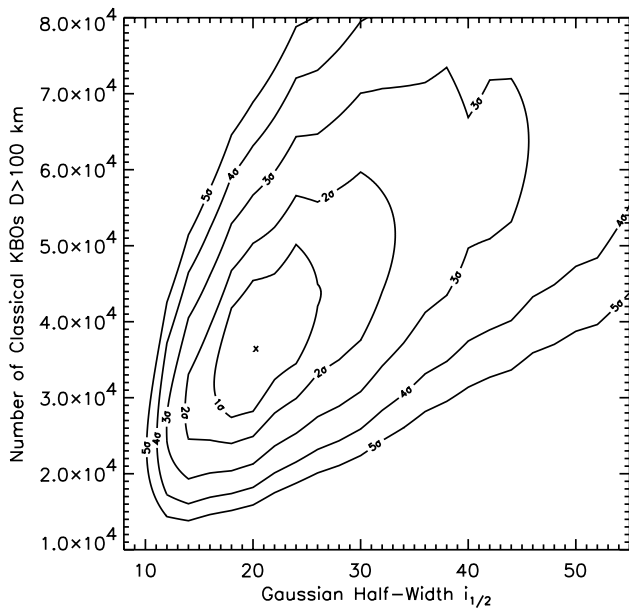


FIG. 12.—Maximum likelihood simulation. Contours of constant likelihood (1, 2, ..., 5 σ) are shown for a model with Gaussian half-width $i_{1/2}$ (x-axis) and total number of CKBOs with diameters greater than 100 km $N_{\text{CKBO}}(D > 100 \text{ km})$ (y-axis). The maximum likelihood occurs at $N_{\text{CKBO}}(D > 100 \text{ km}) = 3.8 \times 10^4$ and $i_{1/2} = 20^\circ$.

objects in the $0^\circ < i < 30^\circ$ range. The Gaussian and flat-top models were equally likely to produce the observed distribution in the 65% confidence limit ($< 1 \sigma$). A Gaussian model multiplied by $\sin i$ was also tried but could be rejected at the greater than 3 σ level because it produced too few low-inclination objects. We also tested the best-fit model

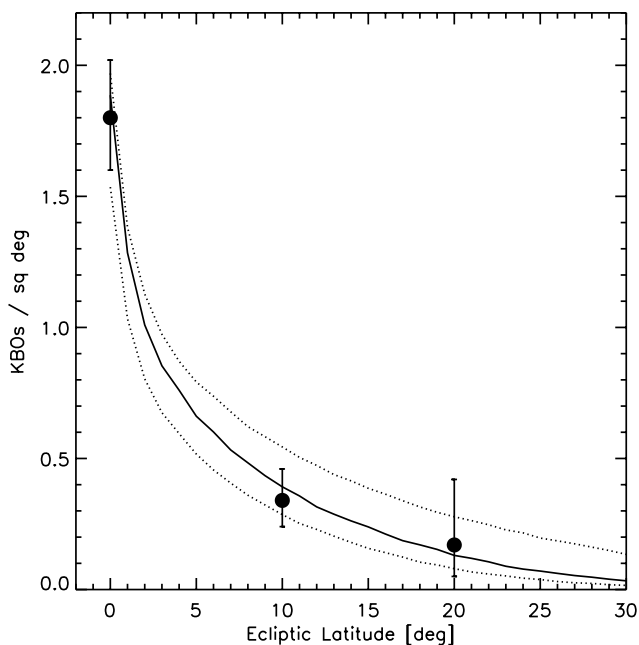


FIG. 13.—Surface density of KBOs brighter than $m_R = 23.7$ vs. ecliptic latitude. The solid line represents the best-fit $i_{1/2} = 20^{+4}_-4$ deg CKBO model, while the dotted lines represent the 1 σ errors. The CKBO model has been multiplied by the observed KBO/CKBO ratio ($86/49 = 1.76$) for display purposes, to simulate the surface density of the more numerous KBOs.

presented by Brown (2001), consisting of two Gaussians multiplied by $\sin i$,

$$\left[a \exp\left(\frac{-i^2}{2\sigma_1^2}\right) + (1-a) \exp\left(\frac{-i^2}{2\sigma_2^2}\right) \right] \sin i, \quad (7)$$

where $a = 0.93$, $\sigma_1 = 2^\circ$, and $\sigma_2 = 18^\circ$, and found it equally compatible with our single Gaussian model (eq. [6]). Because the Gaussian model was the simplest model that fit the observed data well, we chose it to derive the following velocity dispersion results.

We first find the mean velocity vector of all the simulated best-fit CKBOs, \bar{v} , in cylindrical coordinates (normal vectors \hat{r} , $\hat{\theta}$, and \hat{z} representing the radial, longitudinal, and vertical components respectively). The mean velocity vector \bar{v} is consistent with a simple Keplerian rotation model at $R \approx 46$ AU. We then compute the relative velocity of each KBO from this via $|\bar{v} - v_i|$, where v_i is the velocity dispersion contribution of the i th KBO. We find the resulting root mean square velocity dispersion of the \hat{r} -, $\hat{\theta}$ -, and \hat{z} -components to be equal to $\Delta v_r = 0.51 \text{ km s}^{-1}$, $\Delta v_\theta = 0.50 \text{ km s}^{-1}$, and $\Delta v_z = 0.91 \text{ km s}^{-1}$, combining in quadrature for a total velocity dispersion of $\Delta v = (\Delta v_r^2 + \Delta v_\theta^2 + \Delta v_z^2)^{1/2} = 1.16 \text{ km s}^{-1}$. An error estimate of the velocity dispersion can be found by following a similar procedure for the $i_{1/2} = 16^\circ$ and 26° ($\pm 1 \sigma$) models, yielding $\Delta v = 1.16^{+0.25}_{-0.16} \text{ km s}^{-1}$.

4.3. Inferred Mass

The Kuiper Belt mass inferred from these results can be directly calculated from the size distribution and the number of bodies present. For the best-fit $q = 4.0$ size distribution, the mass of CKBOs in bodies with diameters $D_{\min} < D < D_{\max}$ is

$$M(D_{\min}, D_{\max}) = \frac{4}{3} \pi \rho \Gamma \ln(D_{\max}/D_{\min}), \quad (8)$$

where ρ is the bulk density of the object. The normalization constant Γ is calculated from the results of our simulation,

$$\Gamma \approx 3.0 \times 10^{12} m^3 p_R^{-1.5} N(D > 100 \text{ km}), \quad (9)$$

where $N(D > 100 \text{ km}) = 3.8 \times 10^4$ (§ 4.2), yielding $\Gamma = 1.4 \times 10^{19} m^3$ assuming $p_R \equiv 0.04$. The mass for $100 \text{ km} < D < 2000 \text{ km}$ then becomes

$$M(100 \text{ km}, 2000 \text{ km}) \approx 0.03 M_\oplus \left(\frac{\rho}{1000 \text{ kg m}^{-3}} \right) \left(\frac{0.04}{p_R} \right)^{1.5}, \quad (10)$$

where $M_\oplus = 6.0 \times 10^{24} \text{ kg}$ is the mass of Earth. The uncertainties on this value are considerable, as the characteristic albedo and density of the CKBOs are unknown.

4.4. Comparison of the Classical KBOs with Other Dynamical Classes

We found that the total number of CKBOs is given by $N_{\text{CKBO}}(D > 100 \text{ km}) = 3.8^{+2.0}_{-1.5} \times 10^4$. This can be compared with the other main dynamical populations (the resonant and scattered KBOs) from our data. Observational biases favor the detection of the Plutinos over the classical KBOs due to their closer perihelion distance. We found only seven Plutinos (four ecliptic and three off-ecliptic), so we can make only crude (factor of ~ 2) statements about the true size of the population. Thus, we use the results of Jewitt

et al. (1998), who estimate that the apparent fraction of Plutinos (P_a) in the Kuiper Belt is enhanced relative to the intrinsic fraction (P_i) by a factor $P_a/P_i \approx 2$ for $q = 4.0$ and $r_{\max} = 1000$ km. Applying this correction to our ecliptic observations (four Plutinos and 49 classical KBOs) indicates that the total number of Plutinos larger than 100 km in diameter is quite small,

$$N_{\text{Plutinos}}(D > 100 \text{ km}) \approx \frac{4}{4 + 49} \frac{P_i}{P_a} N_{\text{CKBOs}} \approx 1400. \quad (11)$$

The populations of the Plutinos and the 2:1 resonant objects are important measures of the resonance-sweeping hypothesis (Malhotra 1995), which predicts equal numbers of objects in each resonance. Since the 2:1 objects are systematically farther from the Sun than the Plutinos, the true Plutino/2:1 ratio is lower than the observed ratio. Jewitt et al. (1998) estimate the observed/true bias correction factor to be ≈ 0.310 for a survey similar to ours ($q = 4$ and $m_{R50} = 24.0$). Only two of our objects (both found in ecliptic fields) are less than 0.5 AU from the 2:1 resonance, so we find the Plutino/2:1 fraction is given by $(4/2)0.310 \approx 0.6$. Because of the small number of bodies involved, this is only an order-of-magnitude estimate. Within the uncertainties, our observations are consistent with the hypothesis that the 3:2 and 2:1 resonances are equally populated.

The observational biases against the scattered KBOs are considerable. Trujillo et al. (2000) estimate the total population of the scattered KBOs to be $N_{\text{SKBO}}(D > 100 \text{ km}) = 3.1^{+1.9}_{-1.3} \times 10^4$, approximately equal to the population of classical KBOs derived from our data. We summarize the relative populations by presenting their number ratios:

$$\begin{aligned} \text{classical:scattered:Plutino:resonant 2:1} \\ = 1.0:0.8:0.04:0.07. \quad (12) \end{aligned}$$

5. THE EDGE OF THE CLASSICAL KUIPER BELT

We found no objects beyond heliocentric distance $R_{\text{obs}} = 48.9$ AU. There are two possible explanations for this observation: (1) this is an observational bias effect and the bodies beyond R_{obs} cannot be detected in our survey, or (2) there is a real change in the physical or dynamical properties of the KBOs beyond R_{obs} . In order to test these two explanations, we compare the expected discovery distance of an untruncated classical Kuiper Belt with the observations, as depicted in Figure 14. This untruncated CKBO distribution is identical to our best-fit model from § 4.2, except that $40.5 \text{ AU} < a < 200 \text{ AU}$, instead of $40.5 \text{ AU} < a < 46 \text{ AU}$. The total number of bodies produced was considered a free parameter in this model. Inspecting Figure 14, the absence of detections beyond 50 AU is inconsistent with an untruncated model with R^{-2} radial power to the ecliptic-plane surface density. Assuming Poisson statistics apply to our null detection beyond R_{max} , the 99.73% (3σ) upper limit to the number of bodies (μ) expected beyond R_{max} can be calculated from $1 - 0.9973 = \exp(-\mu)$, yielding $\mu = 5.9$ KBOs. We found 49 ecliptic classical KBOs inside the R_{max} limit, so the 3σ upper limit to the number density of KBOs beyond R_{max} is $49/5.9 \approx 8$ times less than the number density of classical KBOs. Although we have constrained the outer edge by the heliocentric distance at discovery R , which is a directly observable quantity, a dynamical edge would be set by the semimajor axes (a) of the object orbits.

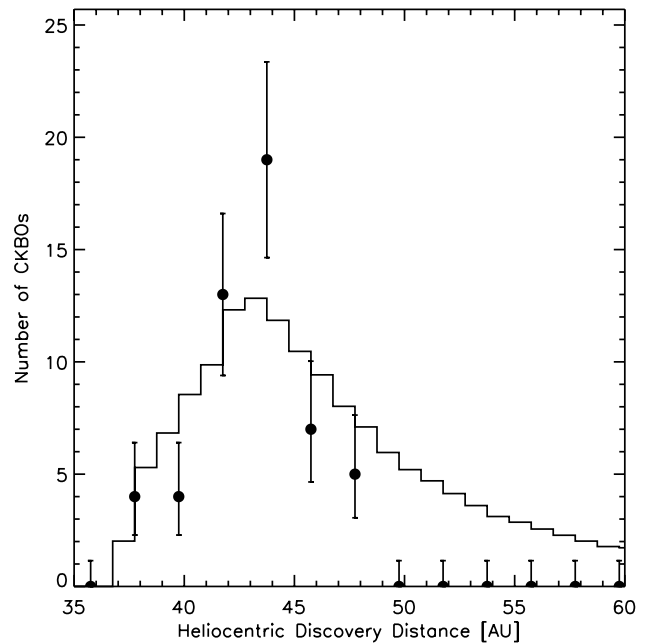


FIG. 14.—Observed heliocentric discovery distance (*data points*) and expected discoveries assuming the best-fit untruncated CKBO model (*solid line*). Note the very sharp drop in discovery statistics beginning at ~ 46 AU, violating the model. This is consistent with an outer edge to the classical Kuiper Belt at 50 AU (3σ).

This difference has little effect on our findings, as the known CKBOs occupy nearly circular orbits with median eccentricity $e = 0.08$ (the calculated median is conservative, as it includes only bodies with $e > 0$ to protect against short-arc orbits, which typically assume $e = 0$). Since an untruncated distribution (explanation 1 above) is incompatible with our data, we must conclude that explanation 2 above applies—there must be a physical or dynamical change in the KBOs beyond R_{max} .

There are several possible physical and dynamical scenarios that could produce the observed truncation of the belt beyond $R_{\text{max}} = 50$ AU (Jewitt et al. 1998): (1) the size distribution of the belt might become much steeper beyond R_{max} , putting most of the mass of the belt in the smallest, undetectable objects; (2) the size distribution could be the same ($q = 4$), but there might be a dearth of large (i.e., bright) objects beyond R_{max} , suggesting prematurely arrested growth; (3) the objects beyond R_{max} may be much darker and therefore remain undetected; (4) the eccentricity distribution could be lower in the outer belt, resulting in the detection of fewer bodies; (5) the ecliptic-plane surface density variation with radial distance may be steeper than our assumed $p = 2$; and (6) there is a real drop in the number density of objects beyond R_{max} . We consider each of these scenarios in turn, and their possible causes.

Detailed simulations of the growth of planetesimals in the outer solar system have not estimated the radial dependence of the formation timescale (e.g., Kenyon & Luu 1999). However, it is expected that growth timescales should increase rapidly with heliocentric distance, perhaps as $t \propto R^3$ (Wetherill 1989). One could then expect a reduction in the number of large objects beyond 50 AU, as per scenario 2 above, and a correspondingly steeper size distribution, as in scenario 1, at larger heliocentric distances. However, with $t \propto R^3$, the timescales for growth at $R = 41$

AU (inner edge) and $R = 50$ AU (outer edge) are only in the ratio 1.8:1. In addition, we observe no correlation between size and semimajor axis among the classical KBOs.

To test scenario 1, we took our untruncated best-fit model and varied the size distribution index q_{out} for bodies with semimajor axes $a > R_{\text{max}}$, keeping the KBO mass across the R_{max} boundary constant. We then found the minimum q_{out} consistent with our null detection beyond R_{max} . This mass conservation model is very sensitive to the chosen minimum body radius r_{min} , because for any $q_{\text{out}} > 4$, most of the mass is in the smallest bodies (Dohnanyi 1969). The minimum size distribution index required as a function of r_{min} appears in Table 12. If mass is conserved for the observable range of bodies, $r_{\text{min}} = 50$ km, the observed edge cannot be explained by a change in the size distribution unless $q > 10$ (3σ), an unphysically large value. For the conservative case of $r_{\text{min}} = 6$ km (roughly the size of cometary nuclei; Jewitt 1997), the observed edge could only be explained by $q > 5.6$ (3σ) beyond R_{max} . We know of no population of bodies with a comparably steep size distribution. Thus, we conclude that the observed edge is unlikely to be solely caused by a change in the size distribution beyond R_{max} .

A similar procedure was followed for scenario 2. Here again, we took our best-fit truncated model and extended it to large heliocentric distances. Then r_{max} was varied to find the largest value that could explain our null detection beyond R_{max} , keeping the total number density of objects with radii $r < r_{\text{max}}$ constant. We found that $r_{\text{max}} < 75$ km (3σ) was required beyond R_{max} to explain the observed edge. This is a factor ~ 5 smaller radius and a factor ~ 150 less volume than our largest object found within R_{max} (1999 CD₁₅₈, ~ 400 km in radius). Such a severe change in the maximum object size beyond R_{obs} would have to occur despite the fact that growth timescales vary by less than a factor of ~ 2 over the observed classical KBO range, as explained above.

One might also expect scenario 3 to be true, as KBO surfaces could darken over time with occasional resurfacing by collisions (Luu & Jewitt 1996), and long growth timescales indicate long collision timescales as well. However, the geometric red albedo would have to be $p_R < 0.008$, a factor 5 lower than that of the CKBOs in our model, assuming a constant number density of objects across the transition region. We are not aware of natural planetary materials with such low albedos.

The dynamical cases, scenario 4 (a drop in the eccentricity distribution) and 5 (a steeper ecliptic-plane density index), can also be rejected. Even an extreme change in the eccentricity distribution cannot explain our observations. Lowering eccentricity from $e = 0.15$ (a high value for the

classical KBOs) to $e = 0$ results in a perihelion change from 42.5 to 50 AU for an object with semimajor axis 50 AU. Such a change corresponds to a 0.7 mag change in perihelion brightness, and to a factor 2.8 change in the surface density of objects expected from our $\alpha = 0.63$ CLF. This model is rejected by our observations at the $> 5\sigma$ level. The variation in ecliptic-plane surface density with respect to heliocentric distance was assumed to follow a power law with index $p = 2$ in our model. However, even a large increase to $p = 5$ would result in a reduction in surface density of a factor 2.7 in the 41 to 50 AU range, which can also be rejected as the cause of our observed edge at the $> 5\sigma$ level.

Since scenarios 1 through 5 seem implausible at best, we conclude that the most probable explanation for the lack of objects discovered beyond R_{max} is scenario 6, the existence of a real, physical decrease in object number density. There have been few works considering mechanisms for such truncation. The 2:1 mean motion Neptune resonance at $a \sim 47.8$ AU is quite close to the observed outer edge of the belt. However, given the Neptune resonance-sweeping model (Malhotra 1995), the resonance could not cause an edge. The sweeping theory predicts that the 2:1 resonance should have passed through the classical Kuiper Belt as Neptune's orbit migrated outward to its present semimajor axis. Thus, the KBOs interior to the current 2:1 resonance ($a \approx 47.8$ AU) could have been affected by this process, but an edge at R_{max} cannot be explained by such a model. Ida et al. (2000) simulate the effect of a close stellar encounter on the Kuiper Belt, suggesting that KBO orbits beyond 0.25–0.3 times the stellar perihelion distance would be disrupted and ejected for a variety of encounter inclinations. Thus, an encounter with a solar mass star with perihelion at ~ 200 AU might explain the observed edge. Such encounters are implausible in the present solar environment but might have been more common if the Sun formed with other stars in a dense cluster.

6. CONSTRAINTS ON A DISTANT PRIMORDIAL KUIPER BELT

While our observations indicate a dearth of objects beyond 50 AU, it is also possible that a “wall” of enhanced number density exists at some large $R \gtrsim 100$ AU distance, as suggested by Stern (1995). We know that the Kuiper Belt has lost much mass since formation, because the present mass is too small to allow the observed objects to grow in the age of the solar system. Kenyon & Luu (1999) found that the primordial Kuiper Belt mass in the $30 \text{ AU} < R < 50 \text{ AU}$ region could have been some $\sim 10 M_{\oplus}$, compared with the $\sim 0.1 M_{\oplus}$ we see today. Stern (1995) also speculated that the primordial surface density may be present at large heliocentric distances. We model this primordial belt as analogous to the CKBOs in terms of eccentricity, inclination, and size distribution, but containing a factor of 100 more objects and mass per unit volume of space. These objects would be readily distinguishable from the rest of the objects in our sample, as they would have low eccentricities characteristic of the CKBOs ($e < 0.25$) yet would have very large semimajor axes ($a > 90$ AU). Since we have discovered no such “primordial” objects, Poisson statistics state that the 3σ upper limit to the sky-area number density of primordial KBOs is 5.9 in 37.2 deg^2 , or 0.16 primordial KBOs per square degree. We constrain the primordial KBOs by allowing the inner edge of the popu-

TABLE 12

MINIMUM q_{out} NEEDED TO EXPLAIN OBSERVED EDGE

r_{min}^a	q_{out}
50.0	10
25.0	7.4
12.5	6.2
6.3	5.6

^a Minimum radius (km) for which mass is conserved across the edge boundary.

lation, a_{\min} , to vary outward, while keeping the outer edge fixed at 250 AU. We find that $a_{\min} = 130$ AU coincides with the 3σ limit on the inner edge of the belt, nearly at the extreme distance limit of our survey. An object discovered at our survey magnitude limit $m_{R50} = 23.7$ at this distance would have diameter $D \approx 1800$ km (approximately 25% smaller than Pluto), assuming a 4% albedo.

7. SUMMARY

New measurements of the Kuiper Belt using the world's largest CCD mosaic array provide the following results in the context of our classical KBO model:

1. The slope of the differential size distribution, assumed to be a power law, is $q = 4.0_{-0.5}^{+0.6}$ (1σ). This is consistent with accretion models of the Kuiper Belt (Kenyon & Luu 1999). This distribution implies that the surface area, the corresponding optical reflected light and thermal emission are dominated by the smallest bodies.

2. The classical KBOs inhabit a thick disk with half-width 20_{-4}^{+6} deg (1σ).

3. The classical KBOs have a velocity dispersion of $1.16_{-0.16}^{+0.25}$ km s⁻¹.

4. The population of classical KBOs larger than 100 km in diameter $N_{\text{CKBO}}(D > 100 \text{ km}) = 3.8_{-1.5}^{+2.0} \times 10^4$ (1σ). The corresponding total mass of bodies with diameters between 100 and 2000 km is $M(100 \text{ km}, 2000 \text{ km}) \sim 0.03 M_{\oplus}$,

assuming geometric red albedo $p_R \equiv 0.04$ and bulk density $\rho \equiv 1000 \text{ kg m}^{-3}$.

5. The approximate population ratios of the classical, scattered, 3:2 resonant (Plutinos), and 2:1 resonant KBOs are 1.0:0.8:0.04:0.07.

6. The classical Kuiper Belt has an outer edge at $R = 50$ AU. This edge is unlikely to be due to a change in the physical properties of the CKBOs (albedo, maximum object size, or size distribution). The edge is more likely a real, physical depletion in the number of bodies beyond ~ 50 AU.

7. There is no evidence of a primordial (factor of 100 density increase) Kuiper Belt out to heliocentric distance $R = 130$ AU.

We thank Dave Tholen and Brian Marsden for providing orbits and ephemerides. We appreciate the vital observational assistance provided by Scott Sheppard and his help with astrometric measurements. We thank David Woodworth, Ken Barton, Lisa Wells, and Christian Vielle for help at the CFHT. We are grateful for the assistance of John Dvorak, Chris Merrick, Lance Amano, Paul DeGroot, and Farren Herron-Thorpe at the University of Hawaii 2.2 m telescope. A NASA grant to D. C. J. provided financial support for this project.

REFERENCES

- Aarseth, S. J., Lin, D. N. C., & Palmer, P. L. 1993, *ApJ*, 403, 351
 Allen, R. L., Bernstein, G. M., & Malhotra, R. 2001, *ApJ*, 549, L241
 Bowell, E., Hapke, B., Domingue, D., Lumme, K., Peltoniemi, J., & Harris, A. W. 1989, in *Asteroids II*, ed. R. P. Binzel, T. Gehrels, & M. S. Matthews (Tucson: Univ. Arizona Press), 524
 Brown, M. E. 2001, *AJ*, 121, 2804
 Brown, M. E., Kulkarni, S. R., & Liggett, T. J. 1997, *ApJ*, 490, L119
 Cellino, A., Zappalà, V., & Farinella, P. 1991, *MNRAS*, 253, 561
 Chiang, E. I., & Brown, M. E. 1999, *AJ*, 118, 1411
 Cochran, A. L., Levison, H. F., Stern, S. A., & Duncan, M. J. 1995, *ApJ*, 455, 342
 Cochran, A. L., Levison, H. F., Tamblin, P., Stern, S. A., & Duncan, M. J. 1998, *ApJ*, 503, L89
 Cuillandre, J.-C., Luppino, G. A., Starr, B. M., & Isani, S. 2000, *Proc. SPIE*, 4008, 1010
 Dohnanyi, J. S. 1969, *J. Geophys. Res.*, 74, 2531
 Dones, L. 1997, in *ASP Conf. Ser. 122, From Stardust to Planetesimals*, ed. Y. J. Pendleton & A. G. G. M. Tielens (San Francisco: ASP), 347
 Duncan, M. J., & Levison, H. F. 1997, *Science*, 276, 1670
 Gladman, B., Kavelaars, J. J., Nicholson, P. D., Lored, T. J., & Burns, J. A. 1998, *AJ*, 116, 2042
 Hahn, J. M., & Malhotra, R. 1999, *AJ*, 117, 3041
 Ida, S., Larwood, J., & Burkert, A. 2000, *ApJ*, 528, 351
 Irwin, M., Tremaine, S., & Żytkow, A. N. 1995, *AJ*, 110, 3082
 Jewitt, D. 1997, *Earth Moon Planets*, 79, 35
 Jewitt, D., & Luu, J. 1993, *Nature*, 362, 730
 Jewitt, D., Luu, J., & Chen, J. 1996, *AJ*, 112, 1225
 Jewitt, D., Luu, J., & Trujillo, C. 1998, *AJ*, 115, 2125
 Jewitt, D. C., & Luu, J. X. 1995, *AJ*, 109, 1867
 ———. 2000, in *Protostars and Planets IV*, ed. V. Mannings, A. P. Boss & S. S. Russell (Tucson: Univ. Arizona Press), 1201
 Kenyon, S. J., & Luu, J. X. 1998, *AJ*, 115, 2136
 ———. 1999, *AJ*, 118, 1101
 Kowal, C. T. 1989, *Icarus*, 77, 118
 Kraft, R. P., Burrows, D. N., & Nousek, J. A. 1991, *ApJ*, 374, 344
 Landolt, A. U. 1992, *AJ*, 104, 340
 Levison, H. F., & Duncan, M. J. 1990, *AJ*, 100, 1669
 Luu, J., & Jewitt, D. 1996, *AJ*, 112, 2310
 Luu, J., Marsden, B. G., Jewitt, D., Trujillo, C. A., Hergenrother, C. W., Chen, J., & Offutt, W. B. 1997, *Nature*, 387, 573
 Luu, J. X., & Jewitt, D. 1988, *AJ*, 95, 1256
 Luu, J. X., & Jewitt, D. C. 1998, *ApJ*, 502, L91
 Malhotra, R. 1995, *AJ*, 110, 420
 Morbidelli, A., & Valsecchi, G. B. 1997, *Icarus*, 128, 464
 Petit, J.-M., Morbidelli, A., & Valsecchi, G. B. 1999, *Icarus*, 141, 367
 Press, W. H., Teukolsky, S. A., Vetterling, W. T., & Flannery, B. P. 1992, *Numerical Recipes in C* (2d ed.; Cambridge: Cambridge Univ. Press), 623
 Sheppard, S. S., Jewitt, D. C., Trujillo, C. A., Brown, M. J. I., & Ashley, M. C. B. A. 2000, *AJ*, 120, 2687
 Stern, S. A. 1995, *AJ*, 110, 856
 Sykes, M. V., & Moynihan, P. D. 1996, *Icarus*, 124, 399
 Tombaugh, C. 1961, in *The Solar System*, Vol. 3, Planets and Satellites, ed. G. P. Kuiper & B. M. Middlehurst (Chicago: Univ. Chicago Press), 12
 Trujillo, C. 2000, in *Minor Bodies in the Outer Solar System*, ed. A. Fitzsimmons, D. Jewitt, & R. M. West (Berlin: Springer), 109
 Trujillo, C., & Brown, M. C. 2001, *ApJL*, in press
 Trujillo, C., & Jewitt, D. 1998, *AJ*, 115, 1680
 Trujillo, C. A., Jewitt, D. C., & Luu, J. X. 2000, *ApJ*, 529, L103
 Wetherill, G. W. 1989, in *The Formation and Evolution of Planetary Systems*, ed. H. A. Weaver & L. Danly (Cambridge: Cambridge Univ. Press), 1